Computational Cosmology: new high redshift galaxy observations

Antonio Aretio Medina

Tutor:

José Oñorbe Bernis

Universidad de Sevilla

Grado en Física

26 de mayo de 2023

Contents

List of Figures

Abstract

When firstly studying the large structure formation from a cosmological perspective it was found that it required the use of simulations to compute the high number of calculations. Nowadays, cosmological simulations are used to discern between different cosmological models through comparison with the observational data. In recent years, Cosmology is entering into an era of precision with goals to drastically reduce the uncertainties of the observations. This will possibly challenge our knowledge of the Universe. In this work, how the newest observations fit inside the current cosmological model has been studied. To do this I have learnt how to use GIZMO by running small cosmological simulations and Rockstar to analyse their results. After this, and using a set of larger simulations, the HMF was obtained and, through an abundance matching with the GSMF from observational data, the stellar-to-halo mass fraction. The observational data at very high redshift used came from the JWST. It was found that the evolution of the HMF and the stellar-to-halo mass fraction was consistent with the current model. On the other hand, the data from the JWST showed bigger stellar masses than what was expected at $z = 10$, showing that star formation should have started before or had been faster than what was thought to be. In conclusion, the JWST data seems to defy the current cosmological model, but the uncertainties do not exclude an agreement between both and more precise observational data is needed to give a clearer answer.

Resumen

Cuando se estudió por primera vez la formación de estructura desde una perspectiva cosmológica, se descubrió que era necesario utilizar simulaciones para realizar los numerosos cálculos. Hoy en día, las simulaciones cosmológicas se utilizan para discernir entre distintos modelos cosmológicos a través de la comparación con los datos observacionales. En los últimos años, la Cosmología está entrando en una era de precisión con objetivos de reducir drásticamente las incertidumbres de las observaciones que posiblemente desafiarán nuestro conocimiento del Universo. En este trabajo se ha estudiado cómo encajan las observaciones más recientes en el modelo cosmológico actual. Para ello he aprendido a utilizar GIZMO ejecutando pequeñas simulaciones cosmológicas y Rockstar para analizar sus resultados. Después de esto, y utilizando un conjunto de simulaciones más grandes, se obtuvo la HMF y, a través de un *abundance matching* con el GSMF a partir de datos observacionales, la fracción de masa estelar-masa halo. Los datos observacionales a muy alto redshift utilizados procedían del JWST. Se encontró que la evolución de la HMF y de la fracción de masa estelar-masa halo era consistente con el modelo actual. Por otro lado, los datos del JWST mostraban masas estelares mayores de lo esperado a $z = 10$, mostrando que la formación estelar debería haber comenzado antes o haber sido más rápida de lo que se pensaba. En conclusión, los datos del JWST parecen desafiar el modelo cosmológico actual, pero las incertidumbres no excluyen un acuerdo entre ambos y se necesitan datos observacionales más precisos para dar una respuesta más clara.

1 Introduction

Since the beginning of the 20$^{\text{th}}$ century, the development of Einstein's theory of general relativity has allowed us to study the evolution of the Universe through time as a dynamical system, allowing modern Cosmology to be included as a branch of Physics and Science. Accompanied by the building of more modern and complex telescopes, cosmologist were able to obtain more precise measurements of the parameters that drive the evolution of the Universe, expanding our knowledge about the mechanisms that made the Universe take the form it has today. At the end of the 20$^{\text{th}}$ century, Cosmology had already accomplished several successes such as the discovery of the expansion of the Universe which led to the development of the Big Bang theory, the characterization of the nature of dark matter or the discovery of dark energy. In less than 80 years, what we knew as the Universe went from being a single galaxy, the Milky Way, to becoming an ever expanding Universe, possibly infinite, and filled with billions of galaxies. But, as the Universe grew, its complexity grew with it.

When studying the Universe large structure it was found that galaxies are not isolated from one another, but that the interactions between them directly participated in their respective evolution. This resulted in the hierarchical structure formation model, where galaxies grow through mergers with smaller ones. This imposed the necessity of using computer simulations to understand how the matter in the Universe organizes itself and how those structures evolve through time in a cosmological context. Although the equations that govern the evolution of the Universe are not complex, inside the high density regions where galaxies are formed they become nonlinear. This led to the introduction of computers and supercomputers in the studies of large scale structure. Since 1974 (Bertschinger, 1998), when the first cosmological simulation to study structure formation was performed, the use of computer simulations of structure formation to test models and make predictions has continued to grow. One of the biggest successes of the cosmological simulations came in 1984 when the hot dark matter model, which proposed that the dark matter was formed by neutrinos, was discarded as the large scale structure formation under that model would have been completely different to the observations (Peebles, 2020, Chapter 7.1).

Computer simulations have proved to be a powerful tool to evaluate cosmological models. In the current one, the Universe is composed fundamentally by dark energy, which affects the rate of expansion of the Universe, dark matter, which only interacts

gravitationally, and baryonic matter, which is the "normal" matter that forms all that we see. Approximately 85% of all matter in the Universe is in the form of dark matter while the rest is baryonic matter. According to this, the most simple cosmological simulation to study the structure formation will be the one that simulates the behaviour of dark matter in an expanding universe. As dark matter only interacts gravitationally, the dynamic of the system will be equal to a N-body simulation with Newtonian gravity. Using different models of dark matter, which are differentiated by, for example, their state equations, will result in a different formation of large scale structure, which allows us to discard dark matter models comparing the results with the observations.

The precision of the observations will directly affect how well It can be discerned between different cosmological models. During the 20^{th} century the precision of the measurements presented errors drifting between 10% and 20%, limiting the models that could be discarded. But this has changed in recent years. More precise instruments like the Planck satellite to study the cosmic microwave background, the Hubble space telescope or the more recent James Webb space telescope among others, have offered more precise measurement of the characteristics of the CMB, the galaxy distribution or their luminosity, allowing to more accurately discern between models that seemed equivalent years before. We are now entering an era of precision Cosmology, where the main goal is to reduce the errors to 1%. If this level of precision is achieved, new studies will possibly end with a more comprehensive understanding of our Universe and its evolution.

The aim of this work is to study the formation and evolution of the large scale structure from a cosmological point of view. This will be achieved through the analysis of different cosmological simulations. In order to do this, I compiled the codes GIZMO and Rockstar, two codes widely used in cosmological studies, to run and analyse a set of simple simulations in my computer. This allowed me to directly observe the operation of both codes and to determine the data of interest that the codes provided. I was not able to use the simulations performed in my computer as they were too simple so that they could be run promptly. Instead, another set of more complex simulations was used. From these simulations, the number density distribution will be obtained as a function of the mass of what is known as dark matter halos, which are basic unit of the large structure. As these halos are stable structures, they obey the virial theorem. Galaxies will form inside the halos, as the will pull gas and dust towards their center, resulting in a relation between

the halos and galaxy density distributions. This relationship between distributions can be found assuming that the most massive halo hosts the most massive galaxy and pairing the rest of galaxies and halos following the same rule. This procedure is called *abundance matching*. The galaxy density distribution can be obtained from observational data, so this will be the link between simulations and observations. Observational results of near and distant galaxies from the Hubble space telescope and of very distant galaxies from James Webb space telescope will be used. From these observational data and the simulation results, the stellar-to-halo mass fraction as a function of the halo mass will be obtained. Analysing the evolution of this parameter with redshift and comparing with the expected evolution, it will be possible to discern how well the newest data from the JWST agree with the current cosmological model.

A brief summary of the structure of this work follows. In section 2, the basis of modern Cosmology and the Λ-CDM model is introduced, followed by an introduction in dark matter halos and large structure formation. In section 3, the methodology followed during this work in order to obtain the halo mass function and the stellar-to-halo mass fraction is described, in addition to a explanation about the operation of the GIZMO and Rockstar codes. In section 4, the results for the halo mass function and the stellar-to-halo mass fraction are presented for the HST and JWST data. In section 5, the conclusions of this work and a discussion of the results is shown.

2 Theoretical framework

2.1 Introduction to Modern Cosmology

To study the behaviour of the Universe as a whole, it is necessary to use Einstein's General Relativity, which describes the gravitational interaction between two massive bodies as a curvature of space-time. Even though Newtonian gravity offers a much simpler theoretical framework to work with, it does not take into account the dynamic natures of space and time. Those magnitudes are neither absolute nor passive as Newton thought, but affect the relative movement between objects in the Universe.

After Einstein published his general theory of relativity, multiple cosmologists tried to describe the Universe and its properties in terms of a space-time metric. One of the first tries came by the hand of Einstein himself, who used his own theory to describe

a stationary and eternal Universe. In order to make his model consistent with general relativity, Einstein had to modify its equations to add a new component that could counter the gravitational attraction and avoid the gravitational collapse in its model. This is known as the Einstein's static universe, which was disproved by observations some years later. The modifications that Einstein introduced in the equations of his theory later became what is now known as dark energy or vacuum energy, as it will be seen later.

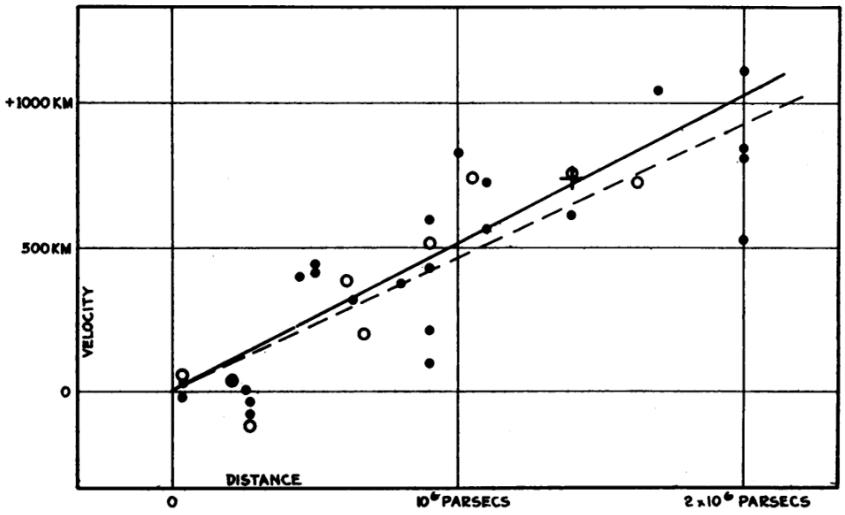

Figure 1: Radial velocities vs. distance for the galaxies observed by Hubble from his original paper. Imagen from Hubble (1929).

In 1927 and 1929, George Lemaître and Edwin Hubble, respectively, observed a linear relation between the radial velocities of galaxies relative to the Milky Way and the distance to them, as shown in figure 1. From these results, Hubble and Lemaître concluded that distant objects' movement follow the equation

$$v = H_0 \cdot D \tag{1}$$

where v is the radial speed of a galaxy, D is the distance between the Milky Way and that galaxy and H_0 is the Hubble's constant at the present. This equation is called the Hubble-Lemaître law. This law was the final proof that disproved Einstein's static universe, as it showed that distances between galaxies changed over time and the Universe could not be in a stationary state.

During the following decades, the determination of the Hubble constant H_0 couldn't be achieved with a high precision. As the value of H_0 directly affects the results, the following

notation was introduced: $H_0 = h \cdot 100$ (km/s)/Mpc, where h is a dimensionless parameter in the interval $0 < h < 1$. Obtaining results as a function of the parameter h helped to make the results independent of the chosen value for H_0. More information about this notation can be found in Croton (2013).

The discovery of the Hubble-Lemaître law provided an observational foothold for other models that predicted an expansion of the Universe. These models form what is known today as the Friedmann-Lemaître-Robertson-Walker metric (FLRW metric). This metric can be derived from the general properties of the Universe, without knowing its content in matter and energy (Weinberg, 2008). The FLRW metric assumed two main properties of the large scale structure of the Universe:

- Homogeneity: there are no privileged points of observation. All observers are equivalent regardless of their position in space.
- Isotropy: There are no privileged directions. The Universe looks the same regardless of the orientation.

These properties are not applicable to every observer, i.e. not every observer will see the Universe as homogeneous and isotropic at its large-scale structure. For example, if an observer A is moving respect to and observer B, and B observes the Universe as homogeneous and isotropic, A will observe that the number density of galaxies measured parallel to its direction of movement is greater than that measured in the perpendicular direction due to the relativistic contraction of distances. Therefore, A won't observe the universe as isotrope. The set of observers that see the Universe as homogeneous and isotrope are called comoving observers, so the FLRW metric is derived from their point of view.

In spherical coordinates, the FLRW metric can be written as

$$ds^2 = dt^2 - a^2(t)\left(\frac{dr^2}{1-kr^2} + r^2(d\theta^2 + \sin\theta d\phi^2)\right) \tag{2}$$

where: $a(t)$ is the scale factor used to convert comoving distances to physical distances. A comoving distance is measured using a scale that expands or contracts with the Universe. Therefore, if two objects maintain a constant comoving distance d_{com} between them, their relative velocities will follow equation 1. The scale factor is normalised to its value at the present time t_0, so $a(t_0) = 1$. It is also related to the Hubble parameter at a given time

$H(t)$ as:

$$H(t) = \frac{\dot{a}(t)}{a(t)} \tag{3}$$

k is a parameter that determines the curvature of space. 3 different geometries are found depending on the sign of k. If $k < 0$ space geometry is hyperbolic. The radial coordinate is not bounded, $r \in [0,\infty]$. When $k = 0$ space geometry is euclidean and the Universe is flat. The radial coordinate is again not bounded. Finally, if $k > 0$ space geometry is spherical and the radial coordinate must take values in the interval $[0,1/\sqrt{k}]$.

This is a general form of the FLRW metric and, apart from the properties of homogeneity and isotropy, it cannot give more specific information about the Universe, such as the curvature factor k or the evolution of the $a(t)$. To know the value and temporal evolution of these parameters it is necessary to introduce the metric in Einstein's field equation to relate it to the energy and matter densities of the Universe.

2.2 Expanding Universe dynamics. Friedmann equations

Einstein's field equation shows a relation between the geometry of space-time and the energy-momentum tensor:

$$R_{\mu\nu} - \frac{1}{2} g_{\mu\nu} R = 8\pi G T_{\mu\nu} \tag{4}$$

where $R_{\mu\nu}$ is the Ricci tensor, defined as an index contraction of the Riemman tensor $R_{\nu\sigma} = R^{\mu}_{\nu\mu\sigma} = \partial_\mu \Gamma^{\mu}_{\nu\mu} - \partial_\sigma \Gamma^{\mu}_{\nu\mu} + \Gamma^{\mu}_{\lambda\mu}\Gamma^{\lambda}_{\nu\sigma} - \Gamma^{\mu}_{\lambda\sigma}\Gamma^{\lambda}_{\nu\mu}$, where $\Gamma^{\mu}_{\nu\rho} = \frac{1}{2} g^{\mu\lambda}(\frac{\partial g_{\lambda\nu}}{\partial x^\rho} + \frac{\partial g_{\lambda\rho}}{\partial x^\nu} - \frac{\partial g_{\nu\rho}}{\partial x_\lambda})$ are the Christoffel symbols, $R = R^{\mu}_{\mu}$ is the Ricci scalar or scalar curvature and $T_{\mu\nu}$ is the energy-momentum tensor, which describes the energy and matter distributions. A more comprehensive introduction of the Einstein's field equation and its relation with the geometry of space-time and the energy content can be found in Weinberg (2008, Chapter 1).

As the Universe is composed of different forms of energy and matter, $T_{\mu\nu}$ can be rewritten as:

$$T_{\mu\nu} = \sum_{\alpha} T^{(\alpha)}_{\mu\nu} \tag{5}$$

where each $T^{(\alpha)}_{\mu\nu}$ is the different component of the total energy and matter density of the Universe. As a good approximation, each component can be treated as a perfect relativistic fluid, i.e. fluids that present no viscosity or heat conduction. For any perfect fluid, it's

energy-momentum tensor must be:

$$T_{\mu\nu} = \begin{pmatrix} \rho & & & \\ & p & & \\ & & p & \\ & & & p \end{pmatrix} \tag{6}$$

where p is the pressure the fluid exerts on its surroundings, which must be equal in all directions to preserve the isometry, and ρ is the energy density. These two magnitudes are related by a equation of state that describe the fluid. It can be assumed that the fluids that are present in the Universe are barotropic, i.e. its density is a function of its pressure $\rho = \rho(p)$. This function can be written as

$$p = \omega\rho \tag{7}$$

where ω is a dimensionless constant that will define the behaviour of the perfect fluid:

- Non-relativistic matter: $\omega = 0 \Rightarrow p = 0$. For this kind of matter, the energy density is much grater than its pressure. In this group, baryonic matter and cold dark matter is found. The baryonic matter is composed of baryons and leptons and is the one which forms the stars, planet, nebulae, etc. On the other hand, dark matter's composition is unknown and it can only be observed by its gravitational effect on the baryonic matter around it as it does not interact electromagnetically.

- Radiation: $\omega = 1/3 \Rightarrow p = \frac{1}{3}\rho$. This applies to electromagnetic radiation and ultra-relativistic particles, such as neutrinos.

- Vacuum energy or dark energy: $\omega = -1 \Rightarrow p = -\rho$. This kind of energy was introduced after the discovery that the expansion of the Universe is accelerating. Its true nature and origin is unknown as of today but its properties can be studied, as explained below.

Upon these three fluids, the $\Lambda - \text{CDM}$ model, also referred to as "standard cosmology", is built. This model takes into account the existence of a cosmological constant Λ which is observed in the form of dark energy. Even though the nature of dark energy is currently unknown, some of its properties can be studied through observation. In this case, the

parameter ω inside the equation of state for dark energy can be determined from the CMB fluctuations. The latest data from the Planck satellite show that $\omega = -1.006 \pm 0.045$ (Planck Collab., Aghanim, et al., 2020), so the approximation $\omega \approx -1$ is valid. CDM means that the model assumes that all dark matter is non-relativistic and behaves as ordinary matter. Other models used hot dark matter (HDM), meaning that it behaved as an ultra-relativistic fluid such as radiation or neutrinos, or warm dark matter (WDM) where it has an intermediate behaviour between an ultra-relativistic and non-relativistic fluid. However, models that included CDM turned out to be closer to what had been observed in simulations of large structure formation, CMB, etc (Peebles, 2020, Chapter 7.1).

The energy-momentum tensor must be conserved, so its divergence div $T = 0$ must be zero. In General Relativity, the divergence of a tensor $T^{\mu\nu}$ is defined as:

$$\text{div } T^{\mu\nu} = T^{\mu\nu}{}_{;\nu} = \partial_\nu T^{\mu\nu} + \Gamma^\mu_{\sigma\nu} T^{\sigma\nu} + \Gamma^\nu_{\sigma\nu} T^{\mu\sigma} \tag{8}$$

Making $\mu = 0$, using equations 3 and 7, and assuming each component of the energy-momentum tensor $T^{(\alpha)}_{\mu\nu}$ is conserved independently to the others, it is obtained obtain

$$T^{0\nu}{}_{;\nu} = \dot{\rho} + 3H\rho(\omega + 1) = 0 \tag{9}$$

Solving this differential equation a relation between the energy density ρ and the scale factor a can be obtained:

$$\rho \propto a^{-3(\omega+1)} \tag{10}$$

Therefore, for the different state equations given previously it is found that the non-relativistic energy density with $\omega = 0$ will evolve as

$$\rho \propto a^{-3} \tag{11}$$

The relativistic energy density with $\omega = \frac{1}{3}$ as

$$\rho \propto a^{-4} \tag{12}$$

and the dark energy with $\omega = -1$ as

$$\rho \propto 1 \tag{13}$$

with the dark energy density being unaffected by the expansion of the Universe. These relations show how the evolution of the scale factor a affects the energy densities in the Universe in different ways according to their behaviour.

Introducing the energy-momentum tensor $T_{\mu\nu} = \sum_\alpha T^{(\alpha)}_{\mu\nu}$ in equation 4, it can be seen that there are only 2 independent equations, as the 3 relations obtained from the spatial components of the tensors must be equivalent due to the isotropy. From the component T_{00}, the following is obtained:

$$\begin{aligned} R_{00} - \frac{1}{2} g_{00} R &= 8\pi G \sum_\alpha \rho^{(\alpha)} \\ \frac{\dot{a}^2}{a^2} + \frac{k}{a^2} &= \frac{8\pi G}{3} \sum_\alpha \rho^{(\alpha)} \end{aligned} \tag{14}$$

This is the Friedmann equation and offers a relation between the temporal evolution of the scale factor a and the energy densities. Using equations 3 and the relations 11, 12 and 13 the Friedmann equation can be rewritten as:

$$H^2 = \frac{8\pi G}{3} \rho_M^0 a^{-3} + \frac{8\pi G}{3} \rho_R^0 a^{-4} + \frac{8\pi G}{3} \rho_\Lambda^0 - \frac{k}{a^2} \tag{15}$$

where the different ρ_i^0 correspond to the energy densities at the present day. Evaluating this equation today (knowing that $a(t_0) = 1$), defining the critical density $\rho_c = \frac{3H_0^2}{8\pi G}$ and the density parameters $\Omega_i = \frac{\rho_i}{\rho_c}$ and $\Omega_k = -\frac{k}{H_0^2}$

$$\Omega_M + \Omega_R + \Omega_\Lambda + \Omega_k = 1 \tag{16}$$

From this relation, it can be inferred how the energy density and the spatial curvature are related. If $\Omega_M + \Omega_R + \Omega_\Lambda = \rho_c$, $\Omega_K = 0$ and the Universe will be flat. If $\Omega_M + \Omega_R + \Omega_\Lambda > \rho_c$, $\Omega_K < 0, k > 0$ and the geometry of the universe is spherical and therefore closed. When $\Omega_M + \Omega_R + \Omega_\Lambda < \rho_c$, the geometry will be hyperbolic and the Universe will be open. An empty Universe ($\Omega_M = \Omega_R = \Omega_\Lambda = 0$) must have hyperbolic geometry.

Finally, the Friedmann equation can be written as

$$\frac{H^2}{H_0^2} = \Omega_M a^{-3} + \Omega_R a^{-4} + \Omega_\Lambda + \Omega_K a^{-2} \tag{17}$$

which can be used to obtain the temporal evolution of the factor scale a for any energy density of the relativistic fluids taken into account. This facilitates the study of certain models, such as the Einstein-de Sitter Universe, which is a flat Universe that only contains matter ($\Omega_R = \Omega_\Lambda = \Omega_K = 0, \Omega_M = 1$), the radiation Universe ($\Omega_M = \Omega_\Lambda = \Omega_K = 0, \Omega_R = 1$), etc. Data from Planck satellite (Planck Collab., Ade, et al., 2016) show that the Universe's densities parameters are:

$$\begin{aligned} \Omega_M &= 0.315 \pm 0.013 \\ \Omega_R &= (9.07 \pm 0.24) \cdot 10^{-5} \\ \Omega_\Lambda &= 0.685 \pm 0.013 \\ \Omega_K &= 0.0007 \pm 0.0019 \end{aligned} \tag{18}$$

These density parameters for the Universe show that it is mostly flat and dominated by matter and dark energy. Radiation energy density is negligible during most part of the history of the Universe, but, as $\rho_R \propto a^{-4}$ while $\rho_M \propto a^{-3}$, there was a time at high redshift when both densities were equal and the contribution of radiation to the expansion was not negligible. That equivalence occurred around $z_{eq} \sim 3400$ (Velten et al., 2014). Regarding the flatness of space, although $\Omega_K \ll 1$ and the approximation to a flat geometry is valid, it shows a small spatial curvature with $k < 0$, which would generate a hyperbolic geometry and an open space. But the absolute error $\Delta\Omega_K > \Omega_K$, so a flat or spherical geometry cannot be discarded.

From the spatial components of equation 4 only one independent relation can be obtained:

$$\begin{aligned} R_{ii} - \frac{1}{2} g_{ii} R &= -8\pi G g_{ii} \sum_\alpha p^\alpha \\ 2\frac{\ddot{a}}{a} + \frac{\dot{a}^2}{a^2} + \frac{k}{a^2} &= -8\pi G \sum_\alpha p^\alpha \\ \frac{\ddot{a}}{a} &= -\frac{4\pi G}{3} \sum_\alpha (1 + 3\omega^{(\alpha)}) \rho^{(\alpha)} \end{aligned} \tag{19}$$

Where the relations 11 to 13 and equation 14 have been used. This is the acceleration equation, and gives information about how the different energy densities affects the rate of expansion. For non-relativistic and ultra-relativistic fluids, with $\omega = 0$ and $\omega = 1/3$, $\frac{\ddot{a}}{a} < 0$ and both fluids will slow the rate of expansion of the Universe. In an Universe with only matter or radiation as contents, the expansion rate will increase at the beginning, $\dot{a} > 0$, but as $\ddot{a} < 0$, it will reach a point where it will start decreasing $\dot{a} < 0$, i.e. the Universe is recollapsing. This is what is commonly known as Big Crunch. In an Universe with only dark energy as content the situation would be different, as $\omega = -1$. $\frac{\ddot{a}}{a} > 0$, so the expansion rate will always grow. As the energy density of dark energy is not diluted by the expansion, the growth will be accelerated. This situation is known as Big Rip.

The Friedmann (14) and acceleration (19) equations are valid in a homogeneous Universe where the energy density is constant in every point of space. But the Universe is homogeneous at large scales, not in smaller scales, as there are celestial bodies such as stars and galaxies. The existence of these bodies is due to the presence of inhomogeneities in the primordial density field. If there were no density inhomogeneities in the early Universe, the gravitational pull on a single particle would be the same in every direction and no larger structure would be formed as matter would not tend to accumulate at any point. The nature of these inhomogeneities in the early Universe will be studied next.

2.3 Inhomogeneities in the early Universe. Structure formation

In 1965, radio astronomers Penzias and Wilson discovered the cosmic microwave background (CMB). They observed a microwave signal that appeared to be isotropic, unpolarized, and not dependent on the moment of measurement which corresponded to a black body radiation with a temperature of 3.5 K (Penzias et al., 1965). 20 years before this discovery, Ralph Alpher, Robert Herman and George Gamow predicted the existence of a radiation background as a result of the recombination of atomic nucleus and electrons approximately 300,000 years after the Big Bang. This event allowed the photons to travel freely as all electric charges where confined in neutral atoms. This moment is called the recombination era. Even though the recombination happened at a high temperature, the expansion of the Universe decreased the photons' energy. They estimated that today's temperature of the CMB today should be around 5 K. It was quickly found that the signal detected by Penzias and Wilson corresponded to the CMB predicted by Alpher, Herman, and Gamow. More

modern measuring of the CMB temperature made by the FIRAS (far Infrared Absolute Spectrophotometer) aboard the WMAP satellite give a result of $T_0 = (2.72548 \pm 0.00057)\ K$ (Fixsen, 2009). A fitting of the CMB spectrum measured by the COBE satellite to a black body emission spectrum can be seen in Figure 2, showing a match between the collected data and a black body spectrum.

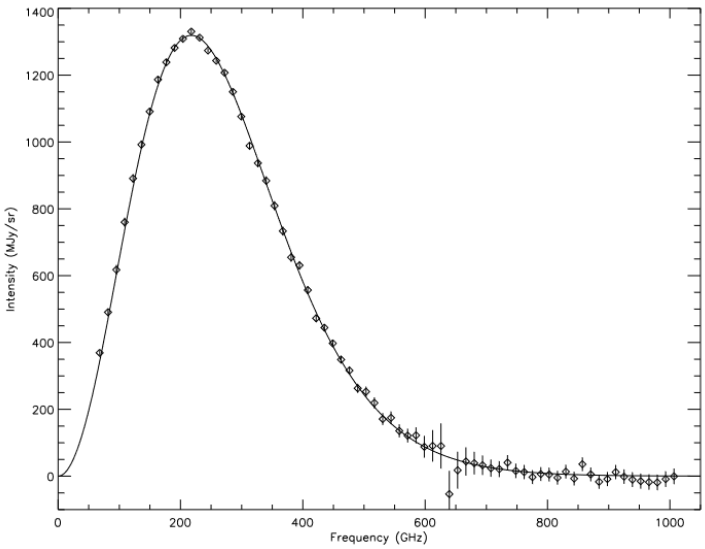

Figure 2: Data from COBE satellite adjusting the intensity as a function of frequency to a black body emission spectrum. Image from Fixsen (2009).

The fact that the radiation temperature is the same independently of the direction of observation shows that all the Universe was in a highly homogeneous state, with all its points having the same energy density. But if that was the case no structure could have been formed, as It was stated previously, as the net gravitational force applied over the matter particles would have been zero. In 1970, James Peebles and J.T Yu determined, using perturbation theory to the FLRW metric, that the CMB must present temperature anisotropies of the order of $\delta T/T \approx 1.5 \cdot 10^{-4}$ with a resolution of 1 minute of arc to form the galaxy clusters observed today (Peebles and Yu, 1970). The temperatures anisotropies of the CMB are closely related to the matter density fluctuations.

In 1989, NASA launched the COBE satellite, which was destined to study the CMB and search for the predicted anisotropies among other objectives. It proved the presence of anisotropies in the CMB compatible with the estimates of Peebles and Yu and, therefore, with the large-scale structure formation. Since the launch of COBE, there have been two other major probes destined to study the CMB: WMAP, launched in 2001, and the most recent was the Planck satellite, launched in 2009. Planck's data build the most detailed

image of the CMB anisotropies up to date, with a resolution of 10 minutes of arch.

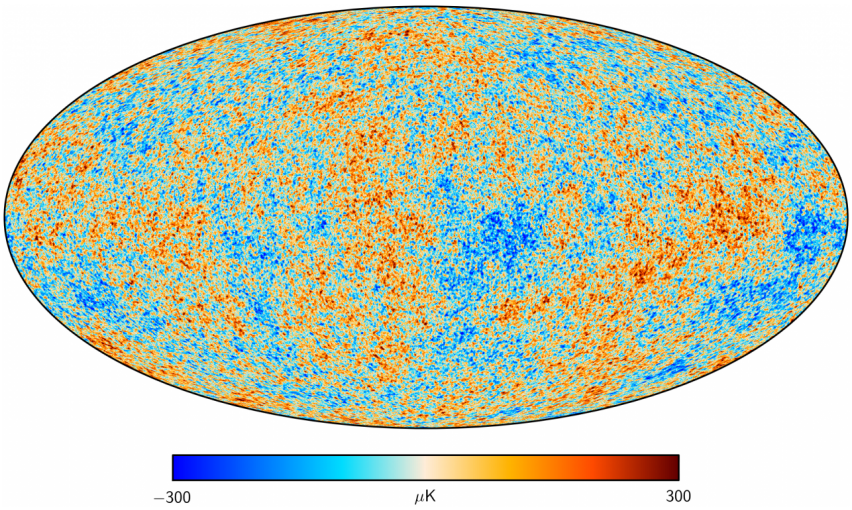

Figure 3: Full-sky map of the temperature fluctuations in the CMB from Planck's data. Image from Planck Collab., Akrami, Y., et al. (2020).

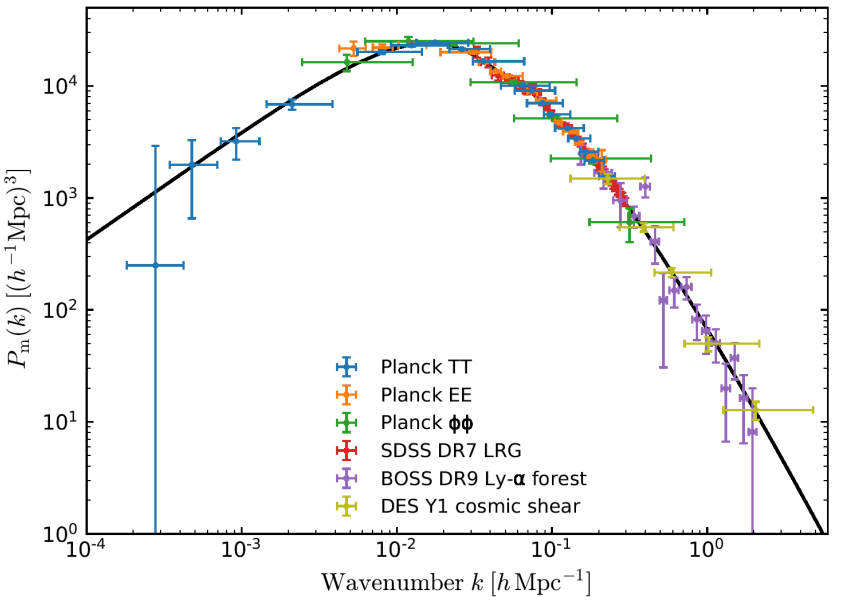

Figure 4: Power spectrum of the primordial density field obtained from CMB data taken from multiple sources. Image from Norman (2010).

The most detailed image of the temperature fluctuations of the CMB was taken by the Planck satellite from ESA which was launched in 2009. Its results are shown in figure 3. The temperature fluctuations of the CMB are related to the density fluctuations present in the Universe at that moment. A higher temperature of the CMB indicates that that region presented a density higher than the mean, while the colder regions correspond to zones less dense than average. When the CMB fluctuations are observed, it is equivalent

to observe a spherical cut of the 3D density field. Then, analysing the CMB fluctuations and applying the principles of homogeneity and isometry, the primordial density field can be obtained. Specifically, the Fourier transform of the primordial density field can be obtained from the multipole expansion in spherical harmonics of the CMB temperature fluctuations. The power spectrum of the primordial density field is shown in figure 4. This power spectrum is usually simplified to a power law function of the form $P(k) = A \cdot k^{-n_s}$ where the parameter n_s defines the power law and A fixes the normalisation of the power law. Observations from Planck show that $n_s = 0.965 \pm 0.004$ (Planck Collab., Aghanim, et al., 2020). The power law normalization is usually given through the parameter σ_8 which corresponds to the amplitude of the matter fluctuations inside a sphere of radius 8 $Mpc\ h^{-1}$. The value of this parameter given by the Planck satellite is $\sigma_8 = 0.811 \pm 0.006$ (Planck Collab., Aghanim, et al., 2020).

2.3.1 Dark matter halos

The collapse dynamic of matter into halos can be simplified by taking into account only the dark matter within the fluid. Dark matter only interacts with itself and other particles through gravity, which simplifies the collapse dynamic. During the formation of halos it is the dark matter the one to create the gravity well, within which ordinary matter will fall to form a galaxy.

Under these circumstances, the formation of dark matter halos (DMH) will be studied. As stated before, a halo is a self-gravitating structure that has decoupled from the expansion of the Universe. As DM must be stable structures, they must follow the virial theorem (Planelles et al., 2014)

$$\langle V \rangle = -2\langle K \rangle \tag{20}$$

where $\langle V \rangle$ is the temporal mean of the gravitational potential energy of the particles and $\langle K \rangle$ is the temporal mean of their kinetic energies. Through the application of the virial theorem, the virial mass M_{vir} and the virial radius r_{vir} of a halo can be defined. r_{vir} is defined as the radius of a sphere within which the mean density is m times the background density, while M_{vir} is defined as the mass inside the sphere of radius r_{vir} (Roos, 2012). The value chosen for m varies between studies as it depends on the approximations taken to study the collapse of an overdensity. During this work, $m = 360$ will be used.

The interaction between halos will be through mergers, where two or more halos collide

and form a single bigger halo. The interaction between a halo and the matter around it is driven by accretion. In the intergalactic medium, there is matter that does not form part of any halo and moves freely through space. If this matter is near a halo, it will fall towards it due to the gravitational pull that the halo exerts over it. Mergers and accretion are the two main interactions that drive the growth and formation of a large-scale structure (Genel et al., 2010).

To study the evolution of halos through time, the halo mass function (HMF) will be used. This function is defined as

$$\phi_{halo}(M_h) = \frac{\mathrm{d}n}{\mathrm{d}\log(M_h)} \tag{21}$$

where n is the number density, i.e. number of halos per volume. This function is expected to decrease at high redshift, as there has not passed enough time for larger halos to form, following the hierarchical structure formation model. An evolution through redshift of the HMF obtained from simulations can be found in Behroozi, Loeb, et al. (2013)

Once a halo is formed in the early Universe, it creates a gravitational well around it due to its mass distribution. Baryonic matter in the form of gas will be attracted towards the center of the halo through accretion. Gas will start to pile up inside it and, eventually, stars will be formed inside it, if enough gas is accreted, and a galaxy will appear. In the early Universe, halos become the seeds of future galaxies, creating a region of space where the gas can decouple from the expansion of the Universe and be able to collapse into stars. As said before, dark matter does not interact with light or matter other than gravitationally. Then, in order to study the properties of the halos, it will be necessary to study the baryonic matter inside of them, i.e. the galaxy hosted inside the halo.

2.3.2 Luminosity-stellar mass relation

As said above, a halo is formed of dark and baryonic matter. The baryonic matter inside the halo will condense inside of it to form a galaxy and will remain in form of dust, gas and stars. All those contribute to the total mass of the galaxy, understood as the baryonic matter component of the halo) and each one of them has to be observed differently..

One of the most direct ways to determine the stellar mass of a galaxy is by studying the light that the galaxy emits. The light spectrum emitted from a galaxy will depend mainly on the stars that form it. Stars can be grouped in stellar populations, which will contain

stars of similar age. Different stellar populations will have different light spectra which will depend on the population. Knowing the spectrum emitted by the chosen populations, it will be possible to adjust a given light spectrum from a galaxy to the number of stars in each population that are present in it. This method is called the *Stellar population synthesis* (SPS) technique, and is widely used in extragalactic astrophysics. An example of this technique can be found in Tamm et al. (2012), where the SPS method is used to obtain the stellar mass distribution of the Andromeda galaxy.

We are interested in obtaining the galaxy stellar mass function (GSMF), which is defined as the number density of galaxies with a given stellar mass. A detailed derivation of the GSMF using the SPS technique over a large number of galaxies is given in Bell et al. (2003). The GSMF can be fitted to a Schechter single function (McLeod et al., 2021)(Bhatawdekar et al., 2019):

$$\Phi(\mathcal{M}) = \Phi^\star \cdot \ln 10 \cdot \left[10^{(\mathcal{M}-\bar{\mathcal{M}}^\star}\right]^{(1+\alpha)} \cdot \exp\left(-10^{\mathcal{M}-\bar{\mathcal{M}}^\star}\right) \tag{22}$$

where $\mathcal{M} = \log(M_\star)$ with $M_\star$ being the galaxy stellar mass, $\bar{\mathcal{M}}^\star = \log\left(\bar{M}_\star\right)$ with $\bar{M}^\star$ being the characteristic stellar mass in solar masses, α the low-mass slope of the GSMF.

3 Methodology

This study of the formation of large-structure in the Universe will rely on cosmological simulations.

During this study, two different codes will be used. First, the simulations are run on GIZMO and the results are analyzed by Rockstar to find halos and determine their masses. The operation of these codes will be explained below.

3.1 Cosmological simulations. GIZMO

In this study, the GIZMO code will be used to run the simulations. More information on its operation and capabilities can be found in Springel (2005) It is a multi-physics simulation code able to calculate the evolution of a system under different conditions. Parting of a basic N-body gravitational simulation, other effects such as hydrodynamical behaviour (viscous fluids), radiative cooling, primordial black holes, etc. can be added.

GIZMO code also allows to include different types of particles in a simulation, allowing to study the evolution of multiple fluids with different behaviours on the same simulation. In addition to it's flexibility, GIZMO also stands out due to its massive parallelisation which, together with its *TreePM* algorithm which will be explained later, allows to run simulations faster and with a more efficient use of computing resources.

This study will focus on N-body simulations of dark matter, added as a collisionless fluid whose particles only interact through gravity. A computer simulation can only work with a finite amount of data, which restricts the simulation to a finite squared volume of size L in comoving coordinates. It can be assumed that the finite box is surrounded by other regions in space with similar properties due to the homogeneity of the Universe. This can be modelled by imposing periodic boundary conditions at the limits of the box. Under these circumstances, the Hamiltonian in comoving coordinates of a system with N particles which interact between them through gravity and are bound to the expansion of the Universe is:

$$H = \sum_i \frac{\vec{p_i}^{\,2}}{2m_i a(t)^2} + \frac{1}{2}\sum_i \frac{m_i \phi(\vec{x}_i - \vec{x}_j)}{a(t)} \tag{23}$$

where $\vec{x}_i$ are the comoving coordinates of the particles and $\vec{p_i}^{\,2} = a^2 m_i \dot{\vec{x}}_i$ are the canonical momenta. $\phi(\vec{x})$ is the gravitational potential given by:

$$\nabla^2 \phi\left(\vec{x}\right) = 4\pi G \left[-\frac{\sum_i m_i}{L^3} + \sum_{i\ \vec{n}} m_i \tilde{\delta}\left(\vec{x} - \vec{n}L\right) \right] \tag{24}$$

where $\vec{n}$ reefers to all triplets of integers $\vec{n} = (n_1,n_2,n_3)$. Note here that $\phi(\vec{x})$ is not the common gravitational potential, as in the density distribution the term $\frac{\sum_i m_i}{L^3}$ is subtracted. This term would correspond to the mean density of the box, so the solution to equation 24 is the *peculiar gravitational potential*

$$\nabla^2 \phi = 4\pi G[\rho(\vec{x}) - \bar{\rho}] \tag{25}$$

In an analytic problem, the Dirac delta function would appear in equation 24, which would lead to the gravitational potential of a point particle $\phi \propto 1/r$. But this potential diverges quickly for small distances, causing very intense forces between two particles that are close to each other and which can lead to computing errors of the accelerations. To solve this problem (introduced purely by the limitations of modern computers) a minimal

distance of interaction ϵ, called softening length, is introduced. If two particles have a distance between the smaller than ϵ, they will not interact gravitationally, eliminating the problem of the divergence of the potential. As it is introduced because of computational, and not physical, reasons, the dynamic at scales smaller than ϵ will not be valid. This is important when the simulations are used to study the internal dynamics or density profile of the halos. As this study will not be of that sort the only concern will be to choose ϵ to be much smaller than the mean distances between halos in the simulations.

In equation 23 it can be seen that to calculate the Hamiltonian function of the system it is necessary to calculate a double sum, resulting in a computational cost of N^2 just to calculate the total gravitational force that is applied over each particle. That is why more complex algorithms are introduced to optimise this process. GIZMO uses an algorithm called the *TreePM* method.

3.1.1 TreePM algorithm

The TreePM method consists in a mixture of two different algorithms: the tree and the particle mesh algorithms. Let us discuss the first one.

The tree algorithm consists of a hierarchical multipole expansion of the box, generating nodes that group the particles together. The partial force generated from a node can be approximated as the force generated by a particle in the centre of the node with a mass equal to all the particles contained inside it. This method can reduce the computational cost as there is no need to calculate $N(N-1)$ partial forces to determine the total force over all the particles, in exchange of obtaining only an approximation of the total forces.

GIZMO code uses an octopole expansion to build the tree. The box of size L (root node) is divided into 8 daughter nodes, which are, in turn, divided again into 8 nodes. This process is repeated until each node only contains a single particle. These are called *leaf* nodes. To determine the force over a particle, GIZMO *walks the tree*. Beginning with the root node, the partial force exerted by the node on a particle is calculated. Then, GIZMO applies a condition to determine if the approximation of the partial force is accurate enough. If it is, the process is terminated and GIZMO continues with other nodes. If not, the node is *opened* and the same process will be applied to the daughter nodes of the current cell. The accuracy of the approximation is determined using the following

condition:

$$\frac{GM}{r^2}\left(\frac{l}{r}\right) \leq \alpha |\,\vec{a}\,| \tag{26}$$

where M is the sum of the masses of the particles inside the node, l is the size of the node and r is the distances to the particle whose acceleration is being determined. $\vec{a}$ is the total acceleration of the particle determined in the last time step and α is the tolerance parameter. If the condition is fulfilled, the approximation is accurate enough and the process continues in the other node.

If the box had non-periodic boundary conditions, the tree algorithm would be enough to obtain an accurate approximation of the total forces, but that is not the case. The periodicity introduces infinite images of the box located around it. As the number of images is infinite, the tree algorithm cannot be used. This is where the particle mesh is applied, which consists of, parting from a grid drawn in the box, calculating approximately the Fourier transformation of the mass distribution and solve the equation 25 in Fourier space

$$\hat{\phi}(\vec{k}) = \frac{4\pi}{k^2}\hat{\rho}(\vec{k}) \tag{27}$$

where $\hat{\phi}$ and $\hat{\rho}$ are the Fourier transforms of the peculiar gravitational potential and the mass distribution respectively.

To apply the TreePM algorithm, the Fourier transformation of the peculiar gravitational potential $\phi_{\vec{k}}$ is divided into a short and long range components

$$\phi_{\vec{k}} = \phi_{\vec{k}}^{short} + \phi_{\vec{k}}^{long} \tag{28}$$

with r_s being the distance where the potential is split and $\vec{k} = (k_x,k_y,k_z)$. The long range potential can be written as

$$\phi_{\vec{k}}^{long} = \phi_{\vec{k}} e^{-\vec{k}^2 r_s^2} \tag{29}$$

where the short range component of the total potential is being truncated by the exponential as high modes are being attenuated. If r_s is chosen to be $r_s \ll L$, equation 24 can be solved in real space for near particles, where $\phi^{short}(\vec{x})$ is

$$\phi^{short}\,(\vec{x}) = -G\sum_i \frac{m_i}{r_i}\,\mathrm{erfc}\left(\frac{r_i}{2r_s}\right) \tag{30}$$

where $r_i = \min(|\vec{x} - \vec{r}_i - \vec{n}L|)$ is defined as the minimal distance from the point $\vec{x}$ to any of the images of the particle i and $\text{erfc}(x)$ is the complementary error function (Kschischang, 2017). It can be seen that the potential of a single particle is the same as in the Newtonian case, but modulated by a complementary error function ($\text{erfc}(x)$) that rapidly attenuates the potential. A tree algorithm can be applied to approximate the gravitational force from the neighbours of a particle as the number of particle and images taken into account is again finite.

To obtain the long range potential $\phi^{long}(\vec{x})$, the Fourier transformation of the mass distribution needs to be determined. To do that, a cell-in-cloud (CIC) assignment is used. CIC calculates an approximation to the density field on a grid structure from a particle distribution. Then, a Fourier transform of the total density distribution $\hat{\rho}(\vec{k})$ can be determined. Using equation 27, applying an inverse Fourier transform to $\hat{\phi}$ and using equation 29, the long range component of the potential $\phi^{long}(\vec{x})$ can be obtained. Once the potentials ϕ^{short} and ϕ^{long} are determined, the partial force generated by both potentials can be calculated using the grid

$$\left.\frac{\partial \phi}{\partial x}\right|_{ijk} \approx \frac{1}{\Delta x}\left(\frac{2}{3}\left[\phi_{i+1,j,k} - \phi_{i-1,j,k}\right] - \frac{1}{12}\left[\phi_{i+2,j,k} - \phi_{i-2,j,k}\right]\right) \tag{31}$$

where $\Delta x = L/N_{mesh}$. The partial force induced by $\phi^{long}(\vec{x})$ is only known in the nodes of the grid so an interpolation between nodes is calculated to obtain an approximation of the force introduced by the long range potential.

3.1.2 Time integration in GIZMO

Another important side of the GIZMO code is the time integration. To evolve the simulations over time, it is necessary to implement an efficient procedure to compute the temporal change of the canonical coordinates of the system. This is achieved through symplectic transformations over the Hamiltonian. More information about these transformations can be found in Quinn et al. (1997).

The usual Hamiltonian function of a N-body system can be divided into a kinetic and potential component: $H = H_{kin} + H_{pot}$. The temporal evolution of each component can

be determined using the following operators

$$D_t\left(\Delta t\right): \begin{cases} \vec{p}_i \;\mapsto\; \vec{p}_i \\ \vec{x}_i \;\mapsto\; \vec{x}_i + \dfrac{\vec{p}_i}{m_i}\displaystyle\int_t^{t+\Delta t} \dfrac{\mathrm{d}t}{a^2} \end{cases} \tag{32}$$

$$K_t\left(\Delta t\right): \begin{cases} \vec{x}_i \;\mapsto\; \vec{x}_i \\ \vec{p}_i \;\mapsto\; \vec{p}_i + \vec{f}_i\displaystyle\int_t^{t+\Delta t} \dfrac{\mathrm{d}t}{a} \end{cases} \tag{33}$$

where $\vec{f}_i$ is the force applied over the particle i. The operator $D_t(\Delta t)$ evolves the kinetic part of the Hamiltonian changing the position but not the canonical momenta, while $K_t(\Delta t)$ evolves the potential part changing the momenta but not the positions. The first is called the *drift* operator while the second is the *kick* operator. Both operators evolve the corresponding coordinates from their value in time t to $t + \Delta t$, where Δt is the timestep. These operators are *symplectic* operators as they are the temporal evolution of the coordinates under each component of the Hamiltonian separately. An approximation of the temporal evolution under the original Hamiltonian H can be written in terms of these two operators:

$$\tilde{U}(\Delta t) = K\left(\frac{\Delta t}{2}\right) D\left(\Delta t\right) K\left(\frac{\Delta t}{2}\right) \tag{34}$$

which is the *kick-drift-kick* (KDK) leapfrog operator. $\tilde{U}(\Delta t)$ is not the exact temporal evolution of the original Hamiltonian H, but it is a symplectic transformation of a modified Hamiltonian $\tilde{H}$. $\tilde{H}$ and H can be related by $\tilde{H} = H + H_{err}$, where:

$$H_{err} = \frac{\Delta t}{12}\left\{\{H_{kin},H_{pot}\},H_{kin} + \frac{1}{2}H_{pot}\right\} + \mathcal{O}(\Delta t^4) \tag{35}$$

where $\{\cdot,\cdot\}$ denotes a Poisson bracket. If $H_{err} \ll H$, the temporal evolution of H and $\tilde{H}$ will be approximately the same, and all the conserved magnitudes in H, like the energy or the angular momentum, will also be approximately conserved in $\tilde{H}$. The conservation of these magnitudes will not be exact. For example, the error Hamiltonian H_{err} will change between timesteps and this will introduce a time dependency in $\tilde{H}$. Although H is time independent and the energy is conserved under it, it will not be conserved under $\tilde{H}$ due to the time dependency introduced by H_{err}. As Δt is chosen for $H_{err} \ll H$ and the temporal evolution of $\tilde{H}$ is similar to that of H, the value of the energy under $\tilde{H}$ will oscillate around

the value of the energy in H.

An alternate form of the approximate temporal evolution operator can be obtained as

$$\tilde{U}(\Delta t) = D\left(\frac{\Delta t}{2}\right) K\left(\Delta t\right) D\left(\frac{\Delta t}{2}\right) \tag{36}$$

called the *drift-kick-drift* (DKD) leapfrog operator. It may seem equivalent to the KDK operator, but its performance in cosmological simulations is lower (Springel, 2005).

The timestep Δt plays a fundamental role in the performance of a cosmological simulation. For a particle that is near a high density region, the acceleration suffered by it will be intense, and for an accurate computation of its trajectory a low timestep will be needed. On the other hand, when a particle is far away from any high density region, its acceleration will not be as intense as before, so the timestep can be larger in order to save computational efforts. A similar argument can be built about the short and long range gravitational forces. Short range forces tend to be more intense and rapidly changing than long range ones, so it is natural to think that short range forces need to be computed more often than long range forces. These two arguments lead us to introduce a variable and adaptive timestep for each particle and type of force.

In a cosmological simulation, the gravitational potential can be separated into two components as shown in equation 28. This leads to the separation of the potential part of the Hamiltonian $H_{pol} = H_{sr} + H_{lr}$. These two new components induces a separation of the *kick* leapfrog operator into a long-range *kick* K_{lr} and a short-range *kick* K_{sr}. With these new operators and having into account the previous arguments, the temporal evolution operator of the simulation can be written as

$$\tilde{U}(\Delta t) = K_{lr}\left(\frac{\Delta t}{2}\right)\left[K_{sr}\left(\frac{\Delta t}{2^m}\right) D\left(\frac{\Delta t}{m}\right) K_{sr}\left(\frac{\Delta t}{2^m}\right)\right]^m K_{lr}\left(\frac{\Delta t}{2}\right) \tag{37}$$

where Δt is a global timestep and m is a positive integer. It can be seen that all possibles timesteps are divisions of the global timestep by powers of 2. That is because a synchronization between particles needs to be maintained. If not, it would add additional temporal asymmetries and it would result in in a worsening of the energy conservation and the result's accuracy.

The time evolution operator in equation 37 is efficient in terms of computational cost. Long range forces need more computational effort than short range ones. The reason is

that to determine long range forces all the particles and its images need to be taken into account and complex mathematical operations take place, while determining short range forces only need to take into account masses in a small region around the particle and is "simpler" mathematically speaking. In the temporal evolution operator, long range forces are only evaluated twice for every particle, while short range ones are evaluated 2^m times.

At the beginning of each iteration, GIZMO applies an acceleration criterion to select the proper timestep for each particle. This is done by assigning the first integer value of m that fulfills

$$\frac{\Delta t}{2^m} \leq \sqrt{\frac{\eta\epsilon}{|\,\vec{a}\,|}} \tag{38}$$

where η is a tolerance parameter, ϵ has dimensions of length that corresponds to the softening length and $\vec{a}$ is the acceleration of the particle in the previous iteration. The parameter Δt is the maximum timestep and its value is chosen by the user. More information on the timestep criteria used in GIZMO can be found in Grudic et al. (2020).

The simulations that will be performed at this study will only contain dark matter particles that will emulate a collisionless dark matter fluid. Even though additional physics can be added to the simulations, in this work they will be limited to pure gravitational N-body simulations. The output of a GIZMO simulation consists of files that contain the coordinates and velocities of each individual particle inside the simulation at a given redshift. Each snapshot also includes critical information about the simulation, value of the cosmological parameters, particle masses, etc.

3.2 Simulation results analysis. Rockstar

Once the simulation results from GIZMO are obtained, they must be analysed as the raw data of the particles positions has no use in this study. The main goal is to study the formation of dark matter halos and their evolution through time, so the interest will be the halos' position and masses. Following the definition of halos given in the theoretical framework, halos will appear as density peaks over a much lower density distribution. Then, obtaining a position of an halo becomes a problem of identifying density peaks.

To obtain density peaks from particle positions, a *friend-of-friends* (FOF) algorithm is commonly used. In a FOF algorithm, a linking length is fixed. Two particles are linked (are *friends*) if the distance between them is less than the linking length. To this another

rule is added: if particle A is linked to particle B, and B is linked to particle C too, then A and C are also linked. Expanding this to a group of particles, groups of linked particles will be obtained. If the linking length of the particles is adjusted correctly, these groups will correspond to density peaks in the distribution. The linking length is typically chosen to be a fraction of the mean density between particles

$$l_{mean} = \alpha \sqrt[3]{\frac{V}{N}},\ \alpha < 1 \tag{39}$$

The, fixing the linking length to a value corresponds to finding density peaks of a certain overdensity value. It is important to note that FOF algorithms will ignore groups with less than a established threshold of for halo particles. This is usually introduced to avoid detecting background noise as a linked group.

The simplicity of the FOF algorithm facilitates its implementation in computer codes, but it is easily seen that it is not enough for a comprehensive study of halos. Its major flaw is the impossibility of studying the internal structure of a halo. For example, the merging of two halos is not an instant process as, during a large part of that process, both halos are well differentiated structures. But, as the density peaks corresponding to both halos are close, the FOF algorithm will count them as one single halo. Another issue is the subhalos, which are halos inside a bigger host. They can be observed in the density distribution as a smaller peak inside a larger one. Again, as FOF algorithm cannot study their internal structure, subhalo masses will be added to the mass of the host halo. This limitation directly affects the results of this study as it artificially modifies the statistic of low mass halos due to a part of them not being accounted for. That is the reason why a more complex code will be used to study, but based upon the FOF algorithm, to analyse the simulation results. This code is *Rockstar*. A complete description of the code can be found in Behroozi, Wechsler, et al. (2012).

Rockstar is an algorithm based on hierarchical FOF groups with an adaptive linking length. Rockstar uses a FOF algorithm in normal space, but also introduces a 6D FOF algorithm in phase space to find overdensities located inside a bigger density peak. By reducing and adapting the phase-space linking length, Rockstar is able to study completely the totality of the overdensity. A shallow description of the code will be shown now.

The first step Rockstar code performs is a FOF algorithm over the particle positions. The linking length used in this phase is defined by the equation 39 with predetermined

value of $\alpha = 0.28$, but it can be modified by the user. The results of this FOF are mainly used for parallelization as the analysis of each individual group can be done by different processors.

In the next stage, a 6D FOF algorithm is run for each FOF group. The phase space is constructed by vectors of the form $\left(\frac{\vec{x}_i}{\sigma_x}, \frac{\vec{v}_i}{\sigma_v}\right)$ where $\vec{x}_i$ and $\vec{v}_i$ are the position and velocity of the particle i and σ_x and σ_v are the position and velocity dispersions of the group to which the particle belongs. The distance between two given particles p_i and p_j is defined as

$$d(p_i,p_j) = \sqrt{\frac{|\vec{x}_i - \vec{x}_j|^2}{\sigma_x^2} + \frac{|\vec{v}_i - \vec{v}_j|^2}{\sigma_v^2}} \tag{40}$$

During this phase the linking length is selected following a different criterion: its value is selected so that a fraction f of all the particles in the group is linked with another particle. To achieve that, the 6D distance between every particle and its closest neighbour is calculated and l_{link} is chosen accordingly. In large groups with more than 10,000 particles, in order not to waste computational effort in determining the linking length, the distances to the closest neighbour are calculated only for 10,000 random particles of the group. Rockstar uses the fraction $f = 0.7$ with a minimum particle threshold of 20. When the 6D FOF algorithm is terminated, Rockstar obtains a 6D FOF group that it's smaller than the original 3D group. This 6D group not only has particles that are relatively close, but also that move similarly. This algorithm is repeated with the new 6D FOF group. The linking length is re-evaluated and adapted to the new group following the same criterion. This process is repeated until the final 6D FOF group contains only 10 particles.

Each run of the 6D FOF algorithm creates a hierarchy between the different subgroups: the deepest levels correspond to the last runs of the 6D FOF algorithm with the closest subgroups to the maximum of the peak, while the shallower levels are the first runs of the algorithm.

To reconstruct an halo from the 6D FOF subgroups, a halo seed is generated at the deepest levels of the hierarchy. As the deepest level corresponds to the closest particles to the maximum of the peak, noise can duplicate a seed halo, which could lead to identification of a duplicate as a substructure when it is not the case. To avoid this, two halo seed will be merged if

$$\sqrt{\frac{|\vec{x}_1 - \vec{x}_2|^2}{\mu_x^2} + \frac{|\vec{v}_1 - \vec{v}_2|^2}{\mu_v^2}} < 10\sqrt{2} \tag{41}$$

where $\mu_i = \sigma_i/\sqrt{n}$. Once all the halo seeds are determined, Rockstar assigns each particle to a halo seed. Starting from the lower subgroups, each particle is assigned to the closest seed in the phase space, defining the distance between a seed and a particle as

$$d(h,p) = \sqrt{\frac{|\vec{x}_h - \vec{x}_p|^2}{r^2_{dyn,vir}} + \frac{|\vec{v}_h - \vec{v}_p|^2}{\sigma_v^2}} \tag{42}$$

$$r_{dyn,vir} = \frac{v_{max}}{\sqrt{\frac{4}{3}\pi G \rho_{vir}}} \tag{43}$$

where v_{max} is the current maximum circular velocity and $\rho_{vir} = 360\rho_m^0$ with ρ_m^0 the simulation background density at $z = 0$ (Bryan et al., 1998). Note that here the virial radius of the halo is used instead of σ_x to ensure that particles assigned to subhalos are close to the main density peak.

Once all halos are reconstructed, Rockstar starts to determine the substructure. This is not a trivial problem as the definition of a host halo and satellite and sub halo can be ambiguous. Given a halo, Rockstar calculates the distance in phase space from it to the more massive halos inside its FOF group. The halo is then assigned to be a satellite halo to the closest more massive halo in phase space.

Before determining the properties of the halo such as its mass or maximum radial velocity, Rockstar runs an algorithm to eliminate unbound particles from the halo. More information about this algorithm can be found in Behroozi, Loeb, et al. (2013), but this is of little interest to this study as, due to the high performance of the 6D FOF algorithm around 98% of particles assigned to a halo are found to be bounded.

Once the halos have been identified and their substructure reconstructed, Rockstar proceeds to calculate the halo properties such as its mass, velocity, maximum rotation velocity, angular momentum, etc. During this study, the property of interests will be halo masses. To determine the mass, the code calculates spherical overdensities using all of the particles contained in the halo. This means that a halo mass will include all the mass assigned to its substructure. Thanks to equation 43 it is well known where a subhalo ends and the host halo begins using its virial radius, so subhalo particles can be adequately isolated from the host halo and the same procedure to determine masses can be used with subhalos. A more detailed description of the approximations done by Rockstar concerning the virial theorem can be found in Bryan et al. (1998).

When Rockstar code is fully terminated, an output is provided. Inside it is contained a list with all found halos and subhalos and their properties (positions, velocities, angular momentum, masses, etc.). All halos are identified with an index number, which is useful, as Rockstar can build merger trees where the halos are identified and can be followed through different snapshots of the simulation. The merger trees will not be used in this study.

3.3 Obtaining the HMF and stellar-to-halo mass fraction

All simulations will be done under the Λ-CDM cosmology, with the density parameters $\Omega_m = 0.285$ and $\Omega_\Lambda = 0.715$, with $h = 0.695$. These simulations will consist in a box with size L filled with N^3 particles. In order to obtain the HMF over a wide range of masses, different box sizes and number of particles will be used. If the lengths and number of particles are chosen correctly, the obtained HMF from a simulation will overlap with other in a certain range of masses, thus enlarging the region where the HMF is obtained. The parameters of each simulation are shown in table 1

L ($Mpc\ h^{-1}$)	N	N_{bin}
10	1024	10
100	256	20
	2048	35
1600	2048	60

Table 1: Box size and number of particles for all simulations used. The number of bins N_{bin} used to construct the HMF from the results is also included.

The simulation with $L = 100\ Mpc\ h^{-1}$, $N = 256$ will only be used at $z = 0$ to obtain the resolution effects, which will be explained later. The other simulations will be evaluated at redshifts $z = 0,3,6,9$ to study the temporal evolution. The simulation with $L = 100\ Mpc\ h^{-1}$, $N = 2048$ will also be evaluated at $z = 10$. From the simulation results, the density distribution of halos as a function of their mass, $\phi_{halo}(M)$, will be obtained. In order to do so, a histogram of the logarithm of halo masses is done and each bin is divided by $L^3 \Delta \log(M_{halo})$ where L is the box size for each simulation and $\Delta \log(M_{halo})$ is the size of each bin. If the bins are sufficiently small

$$\frac{\Delta N/L^3}{\Delta \log(M_{halo})} \approx \frac{\mathrm{d}n}{\mathrm{d}\log(M_{halo})} = \phi_{halo}(M_{halo}) \tag{44}$$

But if bin size is too small, poor statistic effects will accentuate at large masses where the number of halos is small. The number of bins N_{bin} has been chosen for each simulation following these two indications to reduce the effects of poor statistic. The chosen N_{bin} for each simulation is shown in table 1.

All simulations will present a minimum mass resolution fixed by the volume of the box, the number of particles and the cosmological model used. Under a certain mass, the simulations are not able to correctly simulate the halo dynamics due to the approximations taken during the computation of the gravitational forces. Although each simulation has a different minimum mass resolution, that mass corresponds to a fixed number of particles, and a global minimum particle resolution can be found. To determine it, simulations with the same box size but different number of particles will be compared. Changing the number of particles will change the minimum mass resolution, while maintaining the size of the box will assure that both simulations will overlap. The simulations with $L = 100\ Mpc\ h^{-1}$, $N = 2048$ and $L = 100\ Mpc\ h^{-1}$, $N = 256$ will be used. The percentage difference between both simulations will be calculated as:

$$diff(\%) = \frac{|\log(\phi_{2048}) - log(\phi_{256})|}{\log(\phi_{2048})} \cdot 100 \tag{45}$$

Establishing a tolerance tol ≤ 1, the mass at which the divergence starts can be determined as diff$(M_{res}) > 100 \cdot$tol, and the minimum particle resolution can be determined as

$$N_{res} = \frac{M_{res}}{m_p} \tag{46}$$

where m_p is particle mass in the simulation.

To compare the simulation results with the observational data, the number density of halos is transformed into into the stellar-to-halo mass fraction as a function of M_{halo}. This is done by taking the GSMF $\phi_{gal}(M_\star)$ fittings from McLeod et al. (2021) and Bhatawdekar et al. (2019) at the corresponding redshifts and making an abundance matching. This method consists in assuming that most massive halos host the most massive galaxies, which is done analytically by assuming the equivalence between both number density distributions

$$\phi_{halo}(M_{halo}) = \phi_{gal}(M_\star) \tag{47}$$

At very high redshift, fittings from the JWST data from Bouwens et al. (2023) will be used. This study doe not give a fitting of the GSMF, but rather of the luminosity function. The LF represents the number density of galaxies distribution as a function of their absolute magnitude in a certain wavelength band, in the case of Bouwens et al. (2023) the UV band is chosen. The LF is then defined as

$$\phi_{gal}(\mathcal{M}_{UV}) = \frac{\mathrm{d}n}{\mathrm{d}\mathcal{M}_{UV}} \tag{48}$$

where $\mathcal{M}_{UV}$ is the absolute magnitude in the UV band. A relation between $M_\star$ and $\mathcal{M}_{UV}$ will be used in order to obtain the GSMF from the LF. In Stefanon et al. (2021) a linear fitting of the $M_\star$-$\mathcal{M}_{UV}$ is given in the form

$$\log(M_\star) = a \cdot \mathcal{M}_{UV} + b \tag{49}$$

where a and b are the fitting parameters. Using this linear relationship between $M_\star$ and $\mathcal{M}_{UV}$, $\phi_{gal}/M_\star$ can be obtained from $\phi_{gal}(\mathcal{M}_{UV})$ as:

$$\phi_{gal}(M_\star) = \frac{1}{a^2}\phi_{gal}(\mathcal{M}_{UV}) \tag{50}$$

where a is the slope of the linear fitting.

4 Results

In this section, the HMF and stellar-to-halo mass at different redshifts obtained from the different simulations are shown. The first will be calculated using equation 44 while the second will be obtained from the HMF and the GSMF through an abundance matching as explained in section 3. But, before discussing the physics in the results, a previous analysis is needed in order to identify the effects produced by the simulation resolution and own limitations.

4.1 Halo mass functions and their evolution through redshift

In figure 5 the halo mass functions obtained from all available simulations are shown at $z = 0$. It can be seen that, for each simulation, the HMF is obtained in a certain range which depends on the cosmological model used, the size of the box and the number of

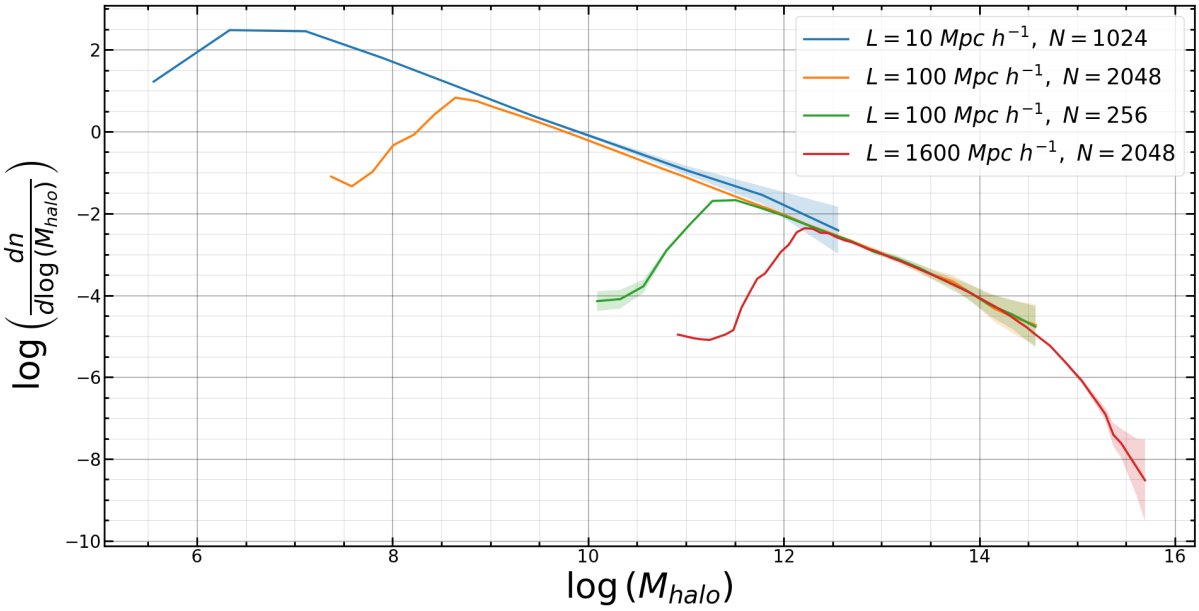

Figure 5: All simulation results at $z = 0$. The convergence between the simulations is broken by the limited resolution of the simulations. This effect will be removed in further analysis. The gap between $L = 100\ Mpc\ h^{-1}$ and $L = 10\ Mpc\ h^{-1}$ simulations is introduced by the too small size of the simulation with $L = 10\ Mpc\ h^{-1}$.

particles. It is important to note how the error bands grow with the mass within the range of each simulation as the number of halos decrease.

Comparing the curves of the two simulations with $L = 100\ Mpc\ h^{-1}$ it is observed that both have the same maximum mass but the simulation with a larger number of particles, $N = 2048$, reaches lower values of M_{halo}. On the other hand, increasing the size of the box L while maintaining constant the number of particles will increase both minimum and maximum masses, as seen comparing the simulations with $L = 100\ Mpc\ h^{-1}$ and $L = 1600\ Mpc\ h^{-1}$ both with $N = 2048$. This is caused because the particle mass m_p increases, allowing the formation of larger halos, but increasing the mass of the smallest halos that can be resolved. Understanding this behaviour is important to determine the best parameters to observe the desired halo mass range and not waste computational effort.

The different curves in figure 5 show an overlap between different simulations over a wide range of masses. The simulation with $L = 10\ Mpc\ h^{-1}$ shows the worst agreement towards the rest. This may be due to the box being too small to offer a good approximation to a real portion of space. Modes larger than $10\ Mpc\ h^{-1}$ of the primordial mass density distribution power spectrum cannot fit inside the box. so the evolution of the matter

fluctuations will be driven by the modes smaller than 10 $Mpc\ h^{-1}$. At high and very high redshift the behaviour of the modes is linear and the absence of larger modes will not affect the evolution of the smaller ones. But, at low redshift, the nonlinear behaviour will arise and the absence of larger modes will cause the divergence between $L = 10\ Mpc\ h^{-1}$ with the rest of simulations. Its convergence will improve at high redshifts, when smaller modes are still linear without being affected by the larger modes.

In figure 5, the HMF from each simulation overlaps with the others until one of them reaches a maximum and suddenly drops at a different mass for each simulation. The point at which the drop occurs is the minimum mass resolution of the simulation. These drops are introduced by the limitations of the simulations to describe halos with a low number of particles. This limitations are introduced by the approximations made during the calculation of the force, such as the softening length of the gravitational potential. These drops will be eliminated in order to keep the mass ranges where the simulations are physically accurate. To characterise this divergences between the simulations, two simulations with the same L but different number of particles N will be used to ensure that both overlap over a large range of masses. The simulations used will both have $L = 100\ Mpc\ h^{-1}$, one will have $N = 2048$ and the other $N = 256$. The percentage difference between both simulations is calculated using equation 45. The minimum mass resolution of the simulation with $N = 256$ will be the mass at which $diff(\%) > \text{tol} \cdot 100$, where tol is an arbitrary tolerance parameter.

As shown in figure 6, the percentage difference between the HMF from both simulations is relatively low at medium masses and increases at low masses. The parameter tol is chosen such that it is not so large that the divergence is still significant, but not so small as to cut off too much of the range where the HMF is physically acceptable. The tolerance was chosen to be $tol = 0.35$, obtaining a minimum particle resolution of $N_{res} = 52.9$. Even though this resolution has been obtained for one simulation, as the other simulations have the same parameters and use the same cosmological model, they will have approximately the same minimum particle resolution. It should also be noted that this result cannot be taken as exact, but as an estimation. To avoid having problems with resolution in larger simulations, the minimum particle resolution for all simulations will be fixed at $N_{res} = 70$

The percentage difference between simulations also increases at large masses, as seen in figure 6. The reason is that all simulations are found to have a low number of large halos,

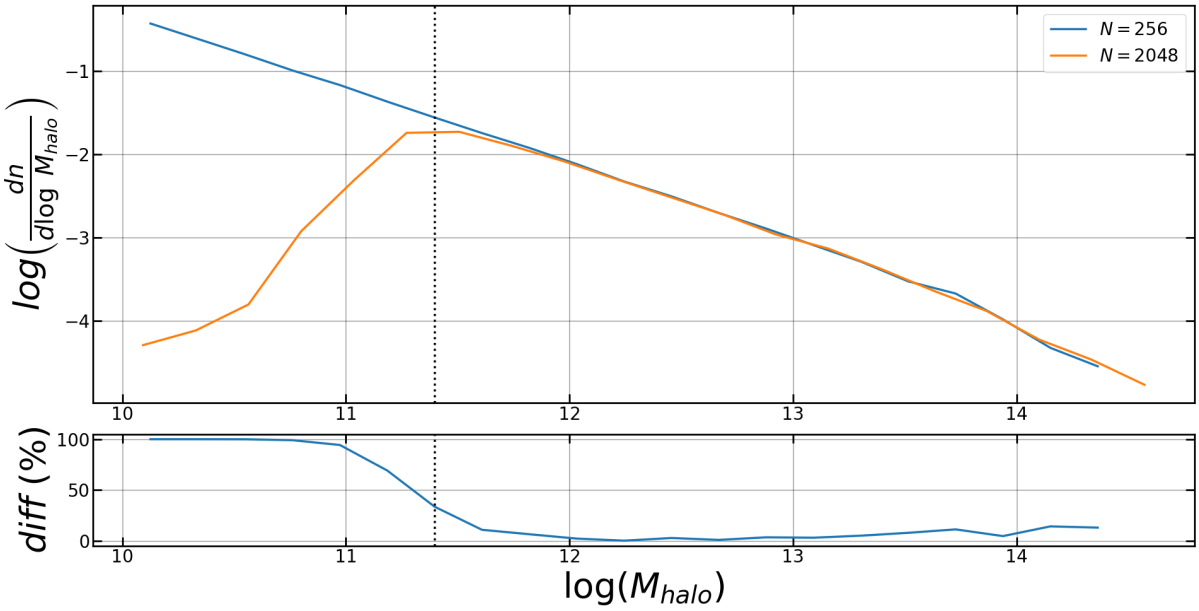

Figure 6: Closer comparison to the halo mass function obtained from simulations with $N = 256$ and $N = 2048$, both with $L = 100\ Mpc\ h^{-1}$. For these results, the percentage difference is represented below. The vertical line marks the first point at which the percentage difference is bigger than $tol \cdot 100$. An increase in the percentage difference can be seen at high masses due to the effects of low statistic.

resulting in a low statistic that will increase statistical errors, reducing the convergence between simulations. This behaviour is expected in the simulations as they are run in a finite box and an infinite number of halos cannot be formed.

In figure 7, it is shown that following the convergence criterion the range within each simulation overlaps with the rest has been obtained. Through this method, the halos below the minimum particle resolution have been removed, obtaining a good agreement between the simulations.

The simulation with $L = 10\ Mpc\ h^{-1}$ still presents the gap between it and the rest of simulations. As explained above, the gap is caused by modes larger than $10\ Mpc\ h^{-1}$ not fitting inside the box and affecting the evolution of smaller modes. To eliminate this gap, a correction was added to the HMF with the form $\phi^*_{L=10} = \phi_{L=10} + \phi_{err}$, where ϕ_{err} is chosen to minimise the percentage difference, calculated using equation 45, between $L = 10\ Mpc\ h^{-1}$ and $L = 100\ Mpc\ h^{-1}$. The result can be seen in figure 8 at $z = 0$. At redshifts $z = 3, 6, 9$ the same procedure has been done, obtaining similar results.

Once all the HMF have been obtained from all the simulations and redshift, the evolution through redshift of each individual simulation will be studied next.

Beginning with the simulation with $L = 1600\ Mpc\ h^{-1}$, $N = 2048$, which reaches the

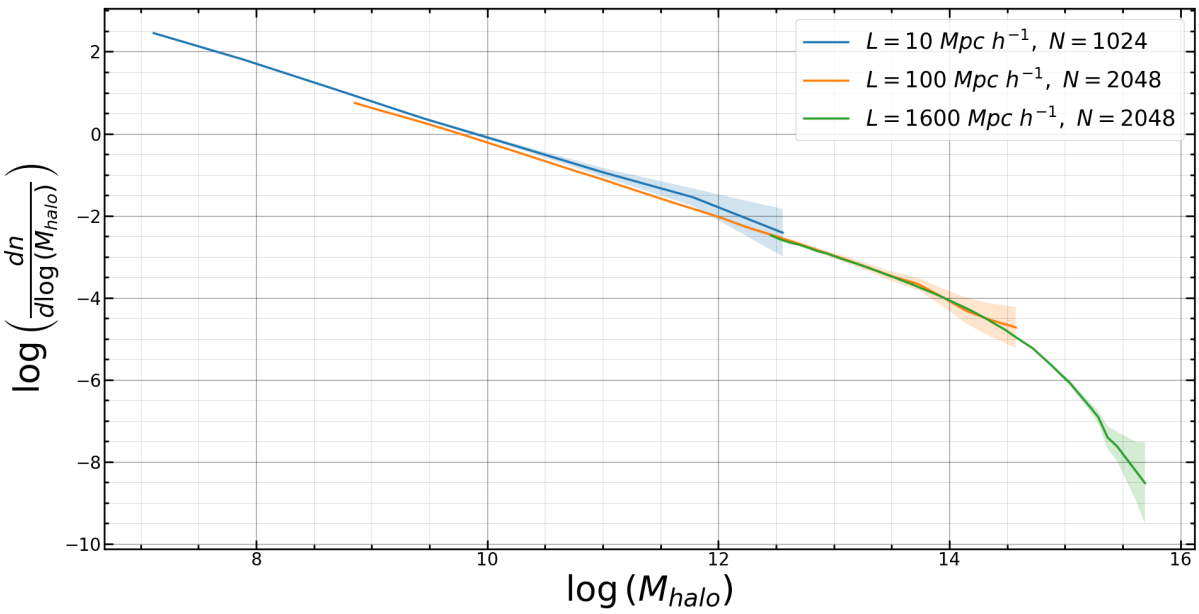

Figure 7: All simulations results at $z = 0$ deleting the masses under the minimum particle resolution $N_{res} = 70$.

highest masses, approximately $10^{16}\ M_\odot$, its evolution is shown in figure 9. At redshift $z = 0$ and $z = 3$ the HMF obtained from this simulation presented good statistic, allowing the statistical errors to be small over a large part of the mass interval. But, at $z = 6$ the statistic is not well enough and the convergence worsens. At $z = 9$ no halos containing more than 70 particles were detected in the simulation and the HMF could not be obtained. This shows that, even though the simulation offered a good statistic of massive halos at $z = 0$ due to its large size and the high number of particles, its minimum particle resolution is too high to be able to accurately represent the halos that existed at $z = 9$. This is again in accordance with the hierarchical structure formation, as it shows that no massive halo was present at high redshift, and once they formed, they must have done it from smaller structures. Due to the poor statistic at $z = 6$, the HMF obtained from that simulation presented wide error bars throughout its range so it was decided not to use that simulation at $z > 3$.

Next,the evolution of the HMF At the lowest masses available will be studied using the simulation with $L = 10\ Mpc\ h^{-1}$, $N = 1024$. In figure 10 the HMF obtained from the simulation with $L = 10\ Mpc\ h^{-1}$, $N = 1024$ is shown at redshifts $z = 0, 3, 6, 9$. The number of halos with masses less than $10^{10}\ M_\odot$ continuously grows from redshift 9 to 3. But it is seen that the HMF at $z = 0$ has a lower slope, intersecting the HMF at $z = 3$ and $z = 6$. This would mean that the number density of the halos below $10^{10}\ M_\odot$ has

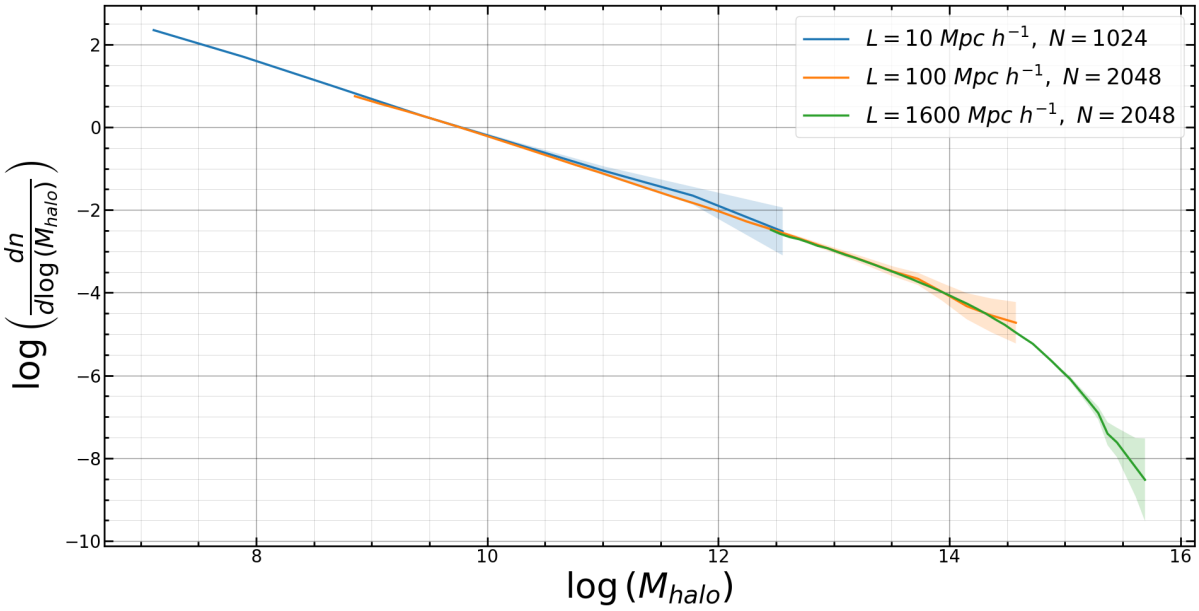

Figure 8: All simulations results at $z = 0$ with a correction of the form $\phi_{10}\prime = \phi_{10} + \delta$ to the simulation with $L = 10\ Mpc\ h^{-1}$ in order to reduce the gap. The correction δ is chosen to minimize the total percentage difference with the simulation with $L = 100\ Mpc\ h^{-1}$.

decreased. Over $10^{10}\ M_\odot$, the HMF at $z = 0$ is larger than the HMF at $z = 3, 6, 9$, so apparently the number density of halos masses larger than $10^{10}\ M_\odot$ keeps growing.

The decrease in the number of halos below $10^{10}\ M_\odot$ could be a result of numerical limitations of the simulations. As was said before, the HMF from $L = 10\ Mpc\ h^{-1}$, $N = 1024$ gave a higher halo density than the rest of the simulations due to its small size. This bigger number of halos could introduce a new dynamical behaviour between halos which would result in a decrease of the number of halos below $10^{10}\ M_\odot$, which would not be shown in other simulations if it was only introduced by the small size of the box. To determine if this is a numerical or physical problem, the HMF obtained from the simulation with $L = 100\ Mpc\ h^{-1}$, $N = 2048$ will be analysed, as it is capable of holding bigger modes of the power spectrum of the primordial density distribution. The HMF obtained from this simulation at redshift $z = 0, 3, 6, 9$ is represented in figure 11, where an intersection between the HMF at $z = 0$ and $z = 3$. The fact that this evolution still appears in this simulation and again around $10^{8.5}\ M_\odot$ reduces the possibilities that this is caused by the limitations of the simulation with $L = 10\ Mpc\ h^{-1}$, $N = 1024$.

As said in the theoretical framework, dark matter halos have two ways of growing: accretion and merging. The accretion, as is the absorption of free particles from the intergalactic medium, will favour the growth of halos at all masses. On the other hand,

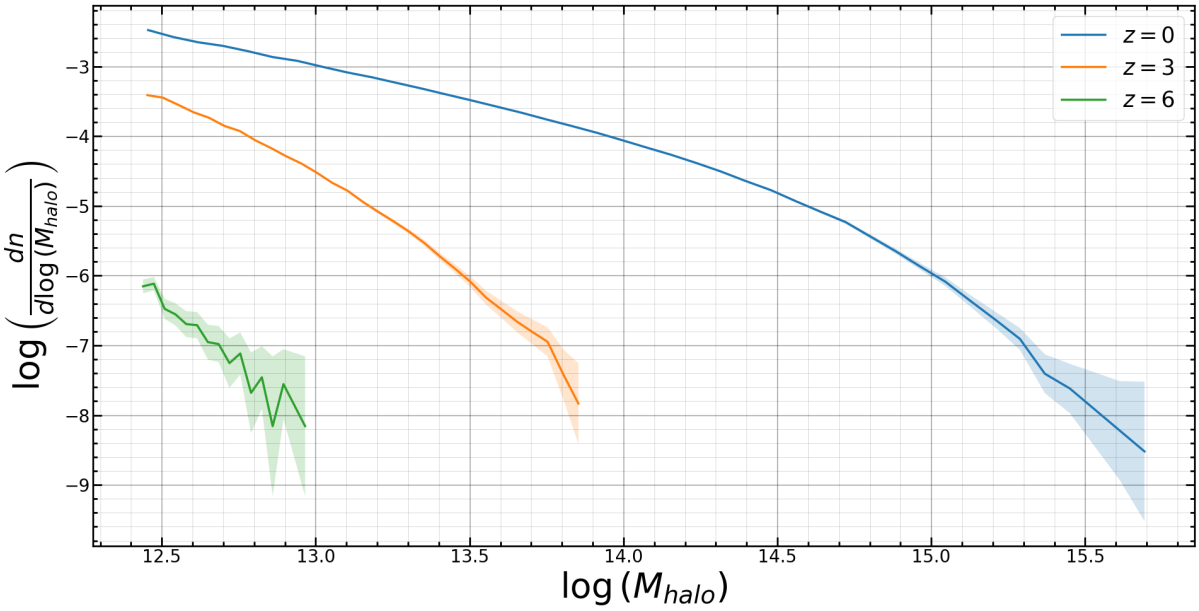

Figure 9: HMF obtained from the simulation with $L = 1600\ Mpc\ h^{-1}$, $N = 2048$ at redshift $z = 0, 3, 6, 9$. It is shown how the convergence towards the HMF is lost at high redshift due to the low number of halos presents in the simulation. Redshift $z = 9$ could not be shown as no halos where found.

mergers are the fastest way for halos to grow. These two process are the two main forces that drive the HMF evolution. At redshifts $z = 9 - 3$, accretion and mergers were the principal mechanism for halos to grow. While mergers led to the rapid growth of halos, accretion allowed for smaller halos to also grow and replace the ones involved in the mergers, allowing for the HMF to increase at all masses. As time passes, the intergalactic medium becomes less dense, diminishing the intensity of accretion, which stopped the replacement of the halos that were involved in mergers. The frequency of mergers also decreased, as the mean distances between halos grew, but were frequent enough to allow the formation of halos above $10^{10}\ M_{\odot}$. As those smaller halos involved in the mergers were not replaced by other halos as the accretion process was negligible, it resulted in a decrease of the number of halos below $10^{10}\ M_{\odot}$.

Once the evolution through redshift of all available simulations has been studied, the global evolution of the HMF within the entire mass range obtained from simulations will be studied. In figure 12, the HMF from all the available simulations is shown for different redshifts. In general, the mass of the largest halo in the simulation decreases as the redshift increases. This means that, at higher redshifts, the halos in the simulations are getting smaller and the mass of the biggest halo found decreases. This indicates that at

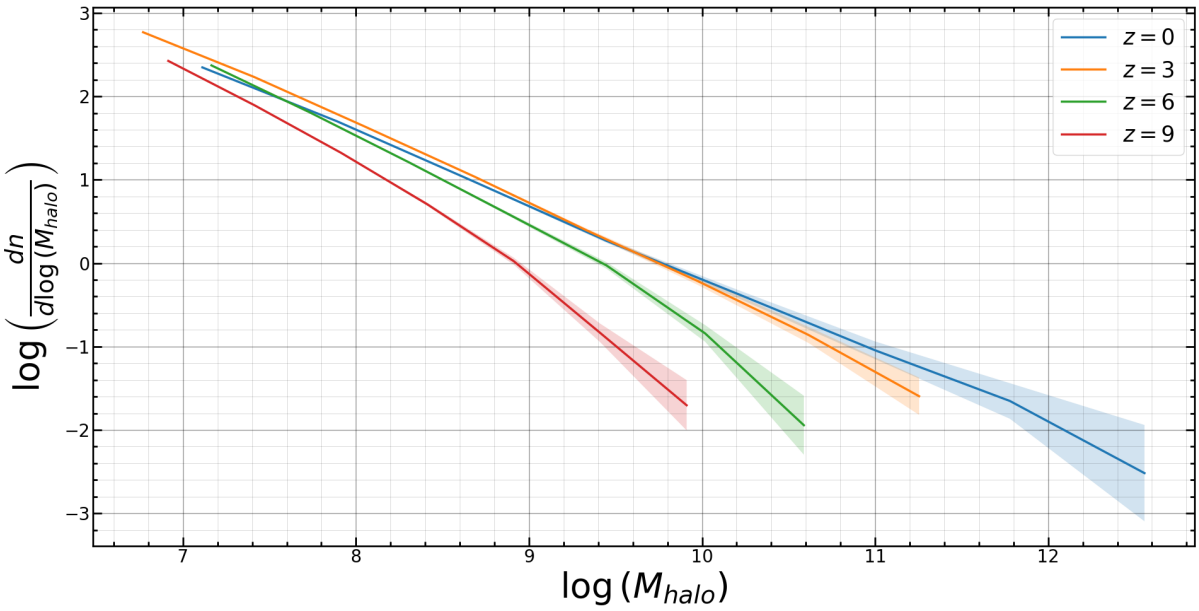

Figure 10: Halo mass function obtained from the simulation with $L = 10\ Mpc\ h^{-1}$, $N = 1024$ at redshifts $z = 0, 3, 6, 9$. This behaviour could be caused by the bad divergence of this simulation.

high redshift there were only low mass halos which, over time, grew through mergers and accretion to form the more massive halos that are found at $z = 0$. This is in agreement with the hierarchical structure formation, which states that smaller halos formed first and then more massive halos could form from smaller structures.

4.2 Stellar-to-halo mass fraction at low and high redshift

Next, the results for the stellar-to-halo mass fractions will be shown and analysed. In order to obtain it, I need to relate the obtained HMF with the observational data through an abundance matching as explained in section 3. Firstly, the stellar-to-halo mass fraction will be obtained at low and high redshift using data from the HST. The results are shown in figure 13 where the stellar-to-halo mass fraction as a function of M_{halo} appears at redshifts $z = 0$. This figure shows that the relation between a halo mass and the mass of the galaxy it hosts is clearly non-linear At $z = 0$, the stellar-to-halo mass fraction starts increasing at masses between $10^{7.5}\ M_\odot$ and $10^{12}\ M_\odot$. It then reaches a maximum between $10^{12}\ M_\odot$ and $10^{13}\ M_\odot$ and falls at masses above $10^{13}\ M_\odot$. the maximum values of the fraction is approximately $M_\star/M_{halo} \approx 10^{-2}$ which means that, at most, the stellar mass of a galaxy represents one-hundredth of the mass of the halo where it is hosted.

If the total baryonic mass of the galaxy was known, there would be a direct observation

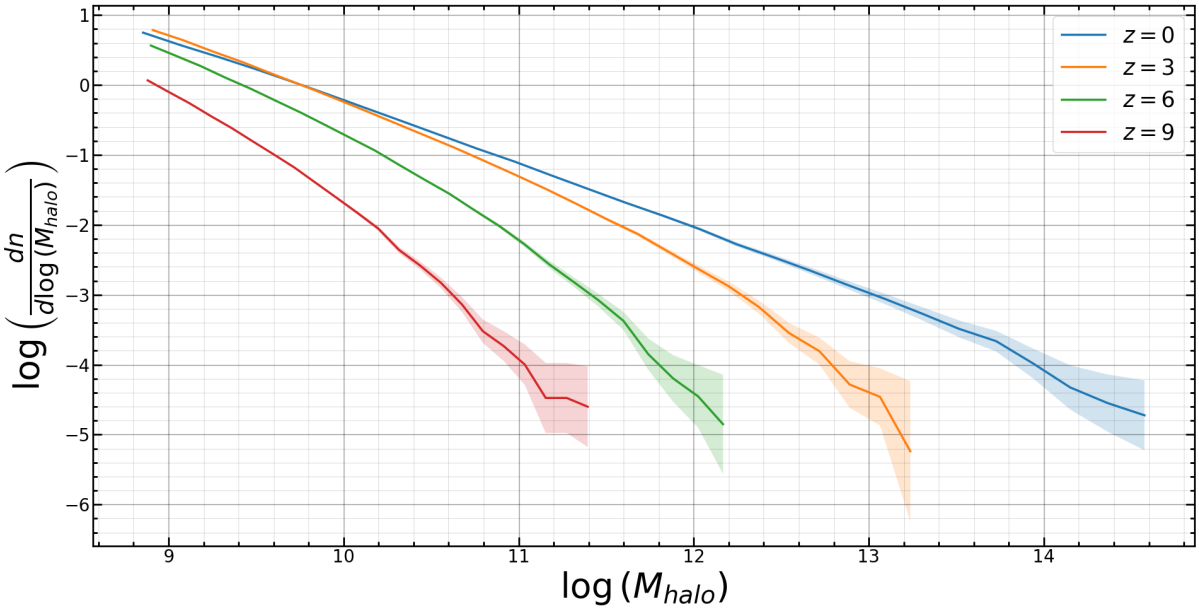

Figure 11: HMF obtained from the simulation with $L = 100\ Mpc\ h^{-1}$, $N = 2048$ at redshifts $z = 0, 3, 6, 9$. At lo masses the intersection between the HMF at $z = 0$ an $z = 3$ is still present, noting that this can't be a behaviour introduced by the simulation with $L = 10\ Mpc\ h^{-1}$. This intersection notes a decreasing of the number of low mass halos introduced by a drop in the accretion rate. at $z = 0$ HMF evolution is driven by mergers.

of how efficient the star formation is in that galaxy, as it would known how much baryonic matter has been turned into stars. It can be assumed that the baryonic-to-dark matter ratio inside a halo is equal to the universal baryonic mass fraction $f_b = \Omega_b/\Omega_m$, where Ω_b is the density parameter of baryonic matter. For the cosmology considered in this work the baryonic fraction has a value of $f_b = 0.156$, in agreement with the observations (Planck Collab., Aghanim, et al., 2020).

Interpreting the figure 13 in terms of stellar formation efficiencies it is direct to see that stellar formation is inefficient at high and low halo masses, while it presents a maximum efficiency between $M_{halo} \sim 10^{12}\ M_\odot$ and $M_{halo} \sim 10^{13}\ M_\odot$. According to Wechsler et al. (2018), at low halo masses, the massive stars that are formed during a starburst are hot enough to heat the gas inside the halo and eject it, preventing the formation of new stars. At high masses, the supermassive black holes located inside the galaxy create an active galactic nucleus (AGN) which heats the gas inside the halo preventing the formation of stars. . At intermediate masses both phenomena decrease their intensities enough to allow the star formation, resulting in a peak of efficiency. This explanation for the behaviour of the stellar formation efficiency with halo masses is a fundamental part of the current model for galaxy formation and evolution and the results follow this behaviour accurately. The

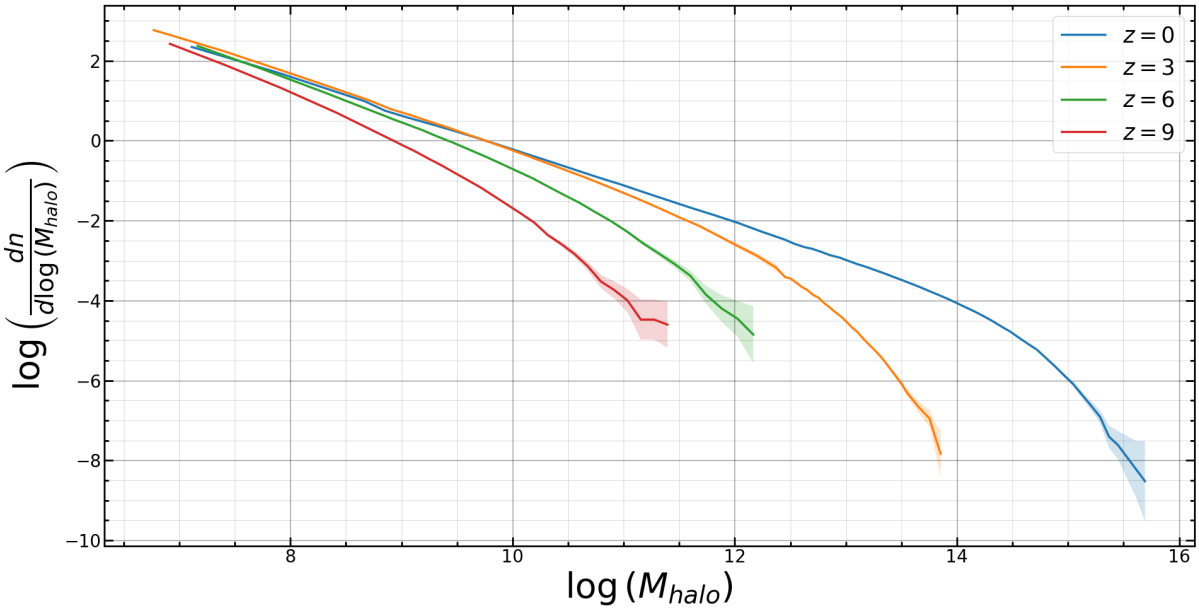

Figure 12: Halo mass function obtained from all simulations at $z = 0, 3, 6, 9$. The simulation with $L = 1600\ Mpc\ h^{-1}$ was excluded due to the low number of halos at high redshift. The evolution of the HMF shows how the number of massive halos reduces with redshift, showing agreement with a hierarchical structure formation model.

maximum of the stellar-to-halo mass ratio is found to be 6% of the baryonic mass fraction. This means that stellar formation is a inefficient process as most part of the baryonic mass inside a galaxy remains in the form of gas. A similar work from Behroozi, Conroy, et al. (2010) showed that the maximum stellar formation efficiency is between 10% and 20%, obtaining a bigger value than mine. A possible cause is the use of different cosmological models. Inn the study of Behroozi, Conroy, et al. (2010) the values used for Ω_m and σ_8 are slightly lower than the values used during this work. Choosing higher values for those parameters accelerates the formation of large scale structure as there is more available matter and the fluctuations are more intense. This will result in a higher number density for halos in the simulations than in Behroozi, Wechsler, et al. (2012). Nevertheless, using the error bands from this study, the results from Behroozi, Conroy, et al. (2010) are at a distance of 2σ from these results. Using the error bands from their study, these results are also at 2σ from theirs. This distance is not statistically significant as, for example, to determine that a discovery has been made it is needed a distance of 5σ.

The stellar-to-halo mass fraction as a function of M_{halo} at redshifts $z = 0, 3, 6, 9$ is shown in figure 14. It can be seen that the end of the mass interval approximately corresponds with the maximum of the stellar formation efficiency, so there is not any

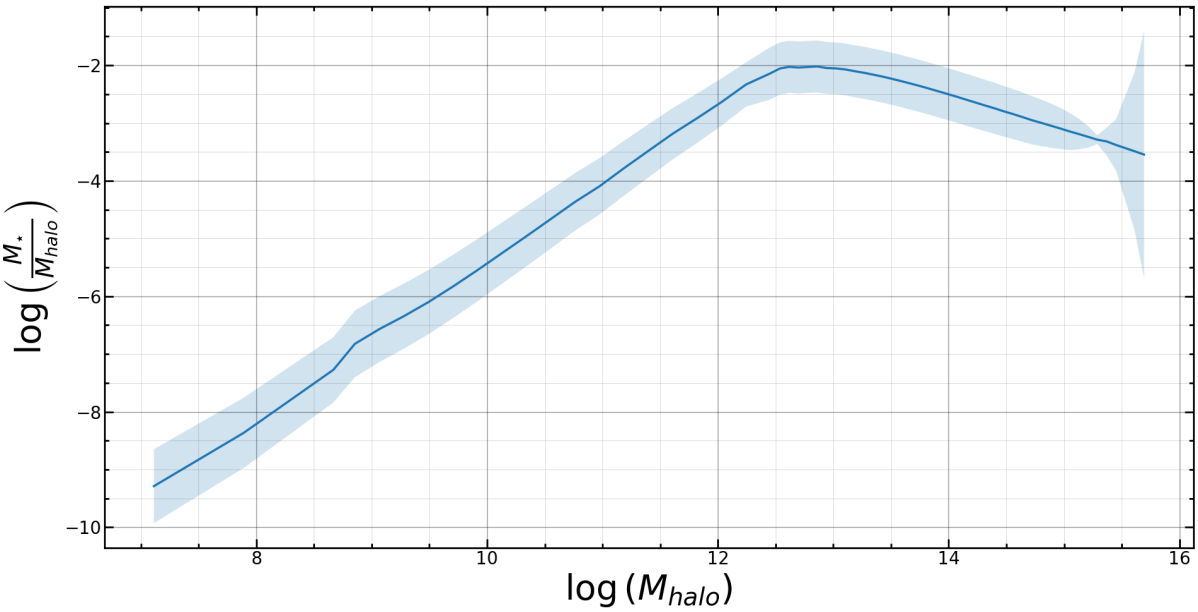

Figure 13: $M_\star/M_{halo}$ fraction as a function of M_{halo} obtained from all available simulations at redshifts $z = 0, 3, 6, 9$. In this figure is shown how the stellar formation efficiency drops at low and high masses due to the gas ejection caused by massive stars at low masses and by the heating of the gas by the AGN at high masses. The peak is reached between $M_{halo} \sim 10^{12}\ M_\odot$ and $M_{halo} \sim 10^{13}\ M_\odot$. The maximum efficiency is approximately the 10% of the baryon fraction.

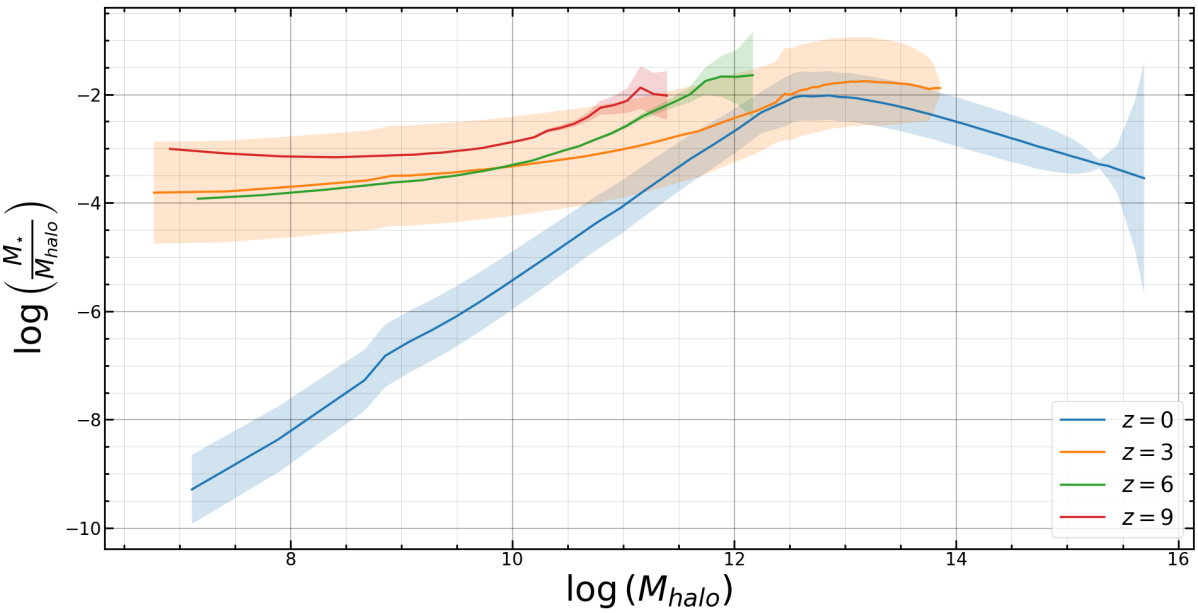

Figure 14: Stellar-to-halo mass as a function of M_{halo} obtained from all simulations at redshifts $z = 0, 3, 6, 9$. The stellar formation efficiency grows at low masses due to the gas accretion that is able to replace the gas the is ejected from the smaller halos.

information of its fall once passed the maximum.

Comparing the stellar-to-halo mass fraction as a function of M_{halo} at different redshifts, it is observed that the stellar-to-halo mass fraction increases with redshift at low masses. As explained before, at low mass halos, once the first stars are formed, gas is expelled of the halo due to the radiation emitted from massive stars. Thanks to the accretion process the expelled gas can be replenished by cold gas from the intergalactic medium allowing that the halo does not expels all the gas. But the accretion rate decreases with redshift (Tillson et al., 2011), leading to a progressive reduction of the available gas for star formation. This, in addition to the fact that stellar formation is an inefficient process, results in a decrease of the stellar mass at low redshift.

The position of the maximum stellar-to-halo mass fraction also varies with the redshift. Starting at $z = 0$, at $z = 3$ it moves to higher masses reaching $10^{13}\ M_{\odot}$. At $z = 6$ and $z = 9$ the maximum drifts to ever lower masses, reaching $10^{12}\ M_{\odot}$ and $10^{11}\ M_{\odot}$ respectively. A similar behaviour with redshift has been observed by Behroozi, Loeb, et al. (2013) where more sophisticated simulations and analysis are used. The position of the maximum is related to the star formation rate inside the galaxies, as at high rates of formation, the factors that blocked star formation are not capable of slowing down the collapse of gas to form a star, resulting in an increase of the mass at which the stellar-to-halo mass fraction peak appears. The star formation rate reached a maximum at redshift $z = 1.9$ (Madau et al., 2014) and has been decreasing ever since until today. This is consistent with the simulation results as the peak is located at a higher mass at $z = 3$ than at $z = 0, 6$ and 9. It is to be expected that the peak reaches a maximum mass around $z = 2$ but, the behaviour of the efficiency at that redshift will not be studied.

The maximum stellar-to-halo mass fraction appears to have small variations, with the redshift always around 10% of the baryonic mass fraction. This light variation shows that star formation is a very inefficient process at all redshifts, leaving the majority of the baryons in the form of gas at a given moment. Simulations of Behroozi, Loeb, et al. (2013) showed approximately the same results, with the maximum efficiency at all redshifts drifting around 10% of the baryonic mass fraction.

In figure 14 a strange behaviour of the stellar-to-halo mass fraction appears at redshift $z = 9$ and below $10^{10}\ M_{\odot}$. It can be seen that there is a change of slope and the fraction a becomes approximately flat around $10^{8.5}\ M_{\odot}$. This behaviour is mostly introduced by

the simulation with $L = 10\ Mpc\ h^{-1}$, $N = 1024$ and has not been observed in any other study, but those simulations did not reach masses that low. This could be caused by the size of the box used in the simulation, which caused a bad convergence of its results towards the HMF. But the stellar-to-halo mass fraction obtained from the simulation with $L = 100\ Mpc\ h^{-1}$, $N = 2048$ at $z = 9$, seems to also flatten around $10^{8.9}\ M_{\odot}$, reducing the possibilities that this is caused by a numerical problem associated with the simulation with $L = 10\ Mpc\ h^{-1}$, $N = 1024$. Similar studies like Behroozi, Loeb, et al. (2013) do not show a change of slope at masses below $10^{10}\ M_{\odot}$ at high redshift, showing instead a constant slope. This behaviour in the results could be introduced by the simulations. This flattening indicates that the number of galaxies grows more rapidly than the number of halos as the halo mass is reduced below $10^{10}\ M_{\odot}$. This could be caused because the simulations are not capable of adequately simulating the number of halos with masses below $10^{10}\ M_{\odot}$.

4.3 Stellar-to-halo mass fraction at very high redshift. JWST data

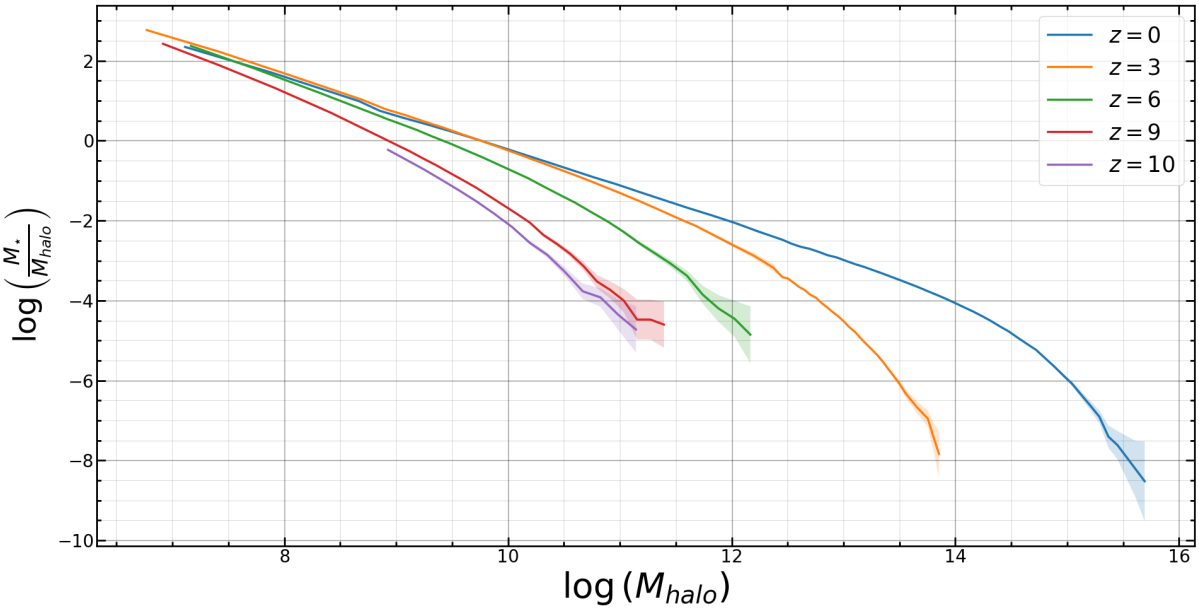

Figure 15: HMF from all simulations at $z = 0, 3, 6, 9, 10$. The HMF that will be used to obtain the stellar-to-halo mass fraction from the JWST data is shown. The HMF at $z = 10$ presents a slight change from the one at $z = 9$ but following the expected evolution.

Finally, after analysing the stellar-to-halo mass fraction at different redshifts, it is possible to compare through the simulations the observational data of the Hubble space

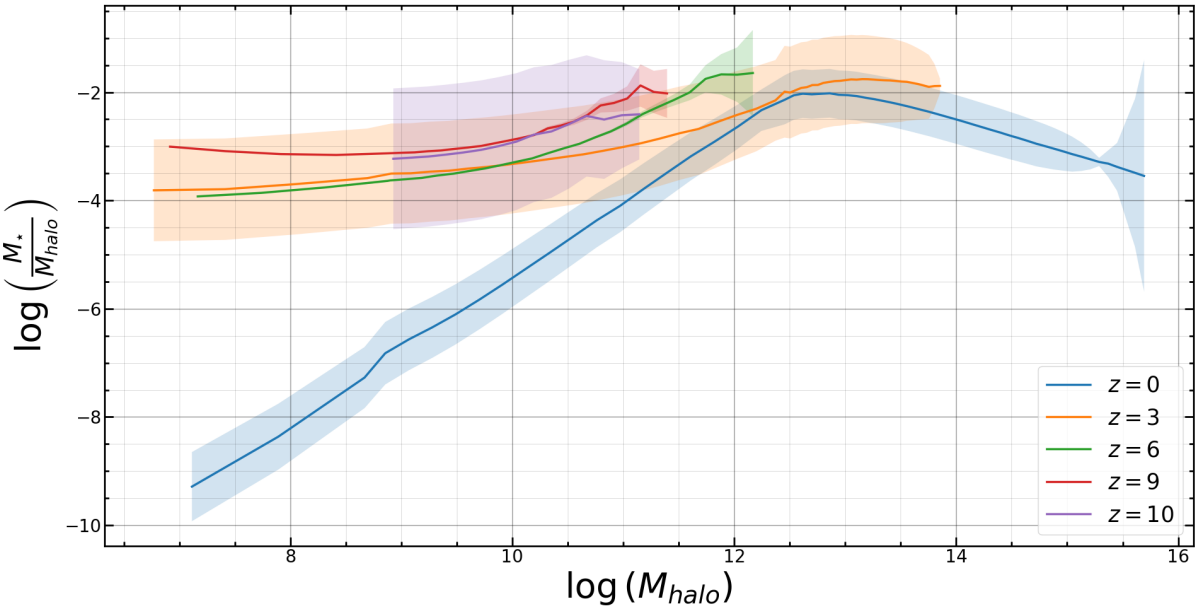

Figure 16: Stellar-to-halo mass as a function of M_{halo} obtained from all simulations at redshifts $z = 0, 3, 6, 9, 10$. The function seems equal to the one at $z = 9$. This could show that the JWST data shows bigger galaxies than those predicted by the current model, as the stellar-to-halo mass fraction should drop as redshift approaches the moment of formation of the first stars.

telescope at $z = 0, 3, 6, 9$ with the ones of the James Webb space telescope at redshift $z = 10$. Firstly, the HMF at $z = 10$ was obtained from the simulation with $L = 100\ Mpc\ h^{-1}$, $N = 2048$. This HMF is shown in figure 15, in comparison with the HMF obtained at redshifts $z = 0, 3, 6, 9$. It can be seen that it shows small variation with the one at $z = 9$. Using this HMF, the stellar-to-halo mass as a function of M_{halo} can be obtained using the data from the JWST and the procedure described in the methodology section. This is shown in figure 16, the stellar-to-halo mass fraction is equal to the one at $z = 9$ showing little change. This means that the GSMF changed slightly, as did the HMF, between the same redshifts. This slow change in the GSMF is not what is expected at high redshift, as it is expected to decrease for redshifts close to the time of formation of the first stars.

The first stars in the Universe formed at the end of what is called the Dark Ages. This period of evolution of the Universe started with the emission of CMB radiation 300,000 years after the Big Bang, and ended with the formation of the first stars 100 million years after the Big Bang, at redshift $z = 20$ (Miralda-Escudé, 2003). This period is called the reionization epoch, where part of the baryonic matter in the Universe transitioned to a state of plasma for the first time since the recombination ob the Big Bang. This was a gradual process as the star formation rate is limited by the gas and dust dynamic inside

a galaxy. The reionization ended around redshift $z = 6$ (Miralda-Escudé, 2003), so it is expected that at a redshift of $z = 10$, the GSMF decreases as the reionization is still in process and there has not been enough time for the stellar formation rate to fully populate the existing galaxies, resulting in a decrease of the stellar-to-halo mass fraction. This is not what is observed in figure 16, where the stellar-to-halo mass fraction remains unchanged from $z = 9$ to $z = 10$. this indicates that the galaxies observed by the JWST have a bigger stellar mass that what our knowledge of the evolution of the Universe predicts.

Taking into account the error bands in the results for the JWST data, it is found that they are wide enough to include a drop in the GSMF and fit within the predictions of the $\Lambda - CDM$ cosmological model. The precision of the results for the stellar-to-halo mass fraction as a function of M_{halo} at $z = 6, 9$ does not help either to the discussion of these results, as the calculated error bars using linear propagation were much bigger than the magnitudes in the results, so they were not plotted in the graphics. Most of the stellar-to-halo mass fraction error bands come from the abundance matching between the HMF from the simulations and the GSMF from the observational data. Therefore, the wide error bands at $z = 10$ come from the fitting of the GSMF at very high redshift. The observations of galaxies at high redshift are very limited as of this moment, resulting in wide statistical errors during the fitting of the GSMF. Although this results are very interesting because they are the first observations of its kind at such a high redshift, they must be taken cautiously due to the limited observations.

5 Conclusion

The aim of this work was to study the formation an evolution of large scale structure. In order to do this the HMF was obtained using equation 44, which defined as the number density of halos as a function of their mass, from 3 main simulations: $L = 10\ Mpc\ h^{-1}$, $N = 1024$, $L = 100\ Mpc\ h^{-1}$, $N = 2048$ and $L = 1600\ Mpc\ h^{-1}$, $N = 2048$. These simulations have been performed using GIZMO and analysed by Rockstar to locate the halos at redshifts $z = 0, 3, 6, 9, 10$. Then, an abundance matching was performed between the HMF from the simulations and the GSMF obtained from observational data at low, high and very high redshift.

It was determined that the minimal particle resolution in the simulations was $N_{res} = 70$,

which allowed us to obtain the HMF in a wide range without divergences between simulations. The effects of poor statistic at the end of the halo mass range of a simulation were also observed. This statistical errors at large masses in a simulation are usually reduced by performing multiple simulations with the same characteristics. Another option is to use a simulations with a larger volume while maintaining constant the minimum mass resolution. This will allow the formation of larger halos, improving the statistic at lower masses.

The simulation with $L = 10\ Mpc\ h^{-1}$, $N = 1024$ presented a gap with the rest of the simulations as the modes of the power spectrum of the primordial density field. This gap was removed through a correction as $\phi'_{10}(M_{halo}) = \phi_{10}(M_{halo}) + \delta$, where δ is a constant chosen as to minimize the percentage difference, calculated using equation 45, with the rest of simulations at each redshift. Using this, it was possible to obtain the HMF as a smooth curve approximately between 10^7 and $10^{16}\ M_\odot$ at $z = 0$.

Comparing it between redshifts it is found that mass of the biggest halo present in the simulations and the HMF at all masses decrease with redshift, which agrees with the hierarchical structure formation model where the smaller structure if formed first and, as time passes, the bigger structure forms through mergers and accretion. This behaviour causes a drastic decrease of the number of halos found in the simulation $L = 1600\ Mpc\ h^{-1}$, $N = 2048$, resulting in a low statistic with wide error bars at $z = 6$ and not finding any halo above $10^{12.4}\ M_\odot$ particles at $z = 9$. An intersection between the HMF at $z = 0$ with $z = 3$ and $z = 6$ which points to a decrease of the lo mass halo number caused by a reduction in the accretion rate, which is in agreement with Tillson et al. (2011). Based on this study, it was determined that between $z = 0$ and $z = 3$ the accretion rate was sufficiently reduced that the HMF evolution was primarily driven by mergers, which causes the intersection between the HMF at $z = 0$ with $z = 3$ and $z = 6$.

To relate the simulation results with the observations, the stellar-to-halo mass fraction as a function of M_{halo} was obtained at different redshifts. This fraction is related to the efficiency of the star formation process, which allows to analyse the star formation within halos of different masses. The stellar-to-halo mass fraction was obtained through an abundance matching between the HMF from the simulations and a set of fittings of the GSMF. The fittings used came from observational data at low redshift ($z = 0, 3$) (McLeod et al., 2021) and at high redshift ($z = 6, 9$) (Bhatawdekar et al., 2019), both obtained from

data of the HST. The results showed a drop of the star formation efficiency at low and high masses, caused by the ejection of gas by the massive stars at low halo masses and by the heating of the gas by an active galactic nucleus at high halo masses, in agreement with Wechsler et al. (2018). The maximum is found between 10^{12} $M_\odot$ and 10^{13} $M_\odot$ reaching 6% of the baryon fraction, showing that star formation is not an efficient process. This maximum efficiency is lower than what was found in a similar study by Behroozi, Wechsler, et al. (2012) where the maximum efficiency was found to be between 10% and 20% of the baryon fraction. Nevertheless, the error bars of this study overlap with the ones from Behroozi, Wechsler, et al. (2012), so both results may be compatible.

Comparing the stellar-to-halo mass fraction at different redshifts, it was observed that the stellar formation efficiency increased at low masses. Based on Tillson et al. (2011), it was determined that this is caused by the accretion of gas towards the halos being more intense at high redshift, allowing the falling gas to replace the one that is being ejected. At low redshift the accretion of gas decreased its intensity (Tillson et al., 2011), preventing that the ejected gas could be replaced. The location of the peak reaches a maximum mass at $z = 3$ and decreases again at $z = 6, 9$ which is in agreement with the star formation rate maximum being at $z = 2.9$, fact observed through direct observation of the star formation process (Madau et al., 2014). Although it is not possible to resolve the peak at high redshift, the maximum efficiency of the star formation process doesn't change substantially being always around the 6% of the baryonic fraction, a lower result than what was found in Behroozi, Wechsler, et al. (2012). This difference could be explained by the use of different cosmological models between this study and theirs. Nevertheless, the distance between both results is not wide enough to be considered statistically significant.

During the redaction of this work, new data at very high redshift from the JWST was released. The first studies analysing these new data showed that the observed galaxies at very high redshift may defy the current cosmological model of galaxy formation and evolution as they apparently have a bigger stellar mass than they should have. It was decided to direct this work towards the comparison of the low and high redshifts from HST with the newer data at very high redshift from JWST. In order to do this, the HMF was obtained at $z = 10$, which showed a small variation from the one at $z = 9$ and following the expected evolution. A luminosity function at very high redshift, $z = 10$, from JWST observational data from Bouwens et al. (2023) was used. To relate the luminosity function

with the GSMF, a linear fitting between the luminosity and stellar masses of galaxies at the same redshift from Stefanon et al. (2021) WAS USED to obtain the stellar-to-halo mass fraction. The resulting function has not changed from the one at $z = 9$, which is not the expected evolution. The first stars in the Universe formed at the beginning of an era called reionization which starter approximately at redshift $z = 20$ (Miralda-Escudé, 2003). This was a gradual process as the star formation rate is limited by the gas and dust dynamic inside a galaxy. The reionization ended around redshift $z = 6$ (Miralda-Escudé, 2003), so it is expected that at a redshift of $z = 10$, the GSMF decreases as the reionization is still in process and there has not been enough time for the stellar formation rate to fully populate the existing galaxies, resulting in a decrease of the stellar-to-halo mass fraction. This is not what is observed in figure 16, where the stellar-to-halo mass fraction remains unchanged from $z = 9$ to $z = 10$. For this galaxies to have these stellar masses, the star formation should have started much earlier. Another possibility is that the first stars were formed when the models predict but the young galaxies had a much bigger star formation rate than what was thought. Either way, this data from the JWST does not seem to show what our knowledge of the evolution of the Universe predicts. Nevertheless, this results must be taken carefully as the luminosity functions introduce large errors due to the low statistic of observed galaxies. The error bars do not completely discard an agreement between the data and the current model. This should motivate new studies when more precise data is released from the JWST.

In order to expand and improve the results of this study it would be necessary to use a wider set of simulations. Although these simulations were conveniently selected to approximately sweep the desired range of halo masses, they resulted to be insufficient to accurately show the maximum of the stellar-to-halo mass fraction. If a simulation with, for example, $L = 600\ Mpc\ h^{-1}$, $N = 2048$, had been available, it would have probably been possible to obtain information of the drop of the stellar efficiency at higher masses than the peak.

About the errors in the stellar-to-halo mass fraction, they are introduced mainly by the fittings of the GSMF and the mass-luminosity relation, so there is nothing that can be done to reduce them. With the current approach of this study the only option is to wait for more precise fittings to be available. More complex simulations that include gas, in order to simulate the baryonic matter distribution and stellar formation, could be used.

With these new simulations, stellar formation could be studied inside halos, allowing a more direct comparison with the observational data, and the use of the fittings could be avoided. But this simulations with stellar formation cannot be simple N-body gravitational simulations, they must be hydrodynamical simulations in order to accurately simulate the behaviour of baryonic matter. This kind of simulations are much more expensive and it would be difficult to use the same volumes and particles that have been used used in this work. An interesting example of studies that includes stellar formation could be Ocvirk et al. (2020), which uses a simulation with $L = 94\ Mpc\ h^{-1}$, $N = 4096$ to study the galaxy formation during the reionization epoch. This simulation needed a long computation time in a supercomputer due to its complexity and size. Because of the high cost of the simulation, it could only be run up to $z = 6$, so no data could be obtained at low redshift.

6 Bibliografía

Behroozi, P. S., C. Conroy, and R. H. Wechsler (2010). "A COMPREHENSIVE ANALYSIS OF UNCERTAINTIES AFFECTING THE STELLAR MASS-HALO MASS RELATION FOR $0 < z < 4$". *The Astrophysical Journal* 717, pp. 379–403.

Behroozi, P. S., A. Loeb, and R. H. Wechsler (June 2013). "Unbound particles in dark matter halos". *Journal of Cosmology and Astroparticle Physics* 2013.06, pp. 019–019.

Behroozi, P. S., R. H. Wechsler, and H.-Y. Wu (Dec. 2012). "THE ROCKSTAR PHASE-SPACE TEMPORAL HALO FINDER AND THE VELOCITY OFFSETS OF CLUSTER CORES". *The Astrophysical Journal* 762.2, p. 109.

Bell, E. F., D. H. McIntosh, N. Katz, and M. D. Weinberg (Dec. 2003). "The Optical and Near-Infrared Properties of Galaxies. I. Luminosity and Stellar Mass Functions". *The Astrophysical Journal Supplement Series* 149.2, pp. 289–312.

Bertschinger, E. (1998). "SIMULATIONS OF STRUCTURE FORMATION IN THE UNIVERSE". *Annual Review of Astronomy and Astrophysics* 36.1, pp. 599–654.

Bhatawdekar, R., C. J. Conselice, B. Margalef-Bentabol, and K. Duncan (Mar. 2019). "Evolution of the galaxy stellar mass functions and UV luminosity functions at z = 6-9 in the Hubble Frontier Fields". *Monthly Notices of the Royal Astronomical Society* 486.3, pp. 3805–3830.

Bouwens, R. J. et al. (Apr. 2023). "Evolution of the UV LF from z∼15 to z∼8 Using New JWST NIRCam Medium-Band Observations over the HUDF/XDF". *Monthly Notices of the Royal Astronomical Society*.

Bryan, G. L. and M. L. Norman (Mar. 1998). "Statistical Properties of X-Ray Clusters: Analytic and Numerical Comparisons". *The Astrophysical Journal* 495.1, pp. 80–99.

Croton, D. J. (2013). "Damn You, Little h! (Or, Real-World Applications of the Hubble Constant Using Observed and Simulated Data)". *Publications of the Astronomical Society of Australia* 30.

Fixsen, D. J. (Nov. 2009). "THE TEMPERATURE OF THE COSMIC MICROWAVE BACKGROUND". *The Astrophysical Journal* 707.2, pp. 916–920.

Genel, S., N. Bouché, T. Naab, A. Sternberg, and R. Genzel (July 2010). "THE GROWTH OF DARK MATTER HALOS: EVIDENCE FOR SIGNIFICANT SMOOTH ACCRETION". *The Astrophysical Journal* 719.1, pp. 229–239.

Grudic, M. Y. and P. F. Hopkins (May 2020). "A general-purpose time-step criterion for simulations with gravity". *Monthly Notices of the Royal Astronomical Society* 495.4, pp. 4306–4313.

Hubble, E. (1929). "A relation between distance and radial velocity among extra-galactic nebulae". *Proceedings of the National Academy of Sciences* 15.3, pp. 168–173.

Kschischang, F. R. (2017). "The complementary error function". *Online, April*.

Madau, P. and M. Dickinson (Aug. 2014). "Cosmic Star-Formation History". *Annual Review of Astronomy and Astrophysics* 52.1, pp. 415–486.

McLeod, D. J. et al. (Mar. 2021). "The evolution of the galaxy stellar-mass function over the last 12 billion years from a combination of ground-based and HST surveys". *Monthly Notices of the Royal Astronomical Society* 503.3, pp. 4413–4435.

Miralda-Escudé, J. (2003). "The Dark Age of the Universe". *Science* 300.5627, pp. 1904–1909.

Norman, M. L. (2010). *Simulating Galaxy Clusters*.

Ocvirk, P. et al. (Aug. 2020). "Cosmic Dawn II (CoDa II): a new radiation-hydrodynamics simulation of the self-consistent coupling of galaxy formation and reionization". *Monthly Notices of the Royal Astronomical Society* 496.4, pp. 4087–4107.

Peebles, P. J. E. (2020). *Cosmology's Century: An Inside History of Our Modern Understanding of the Universe*. Princeton University Press.

Peebles, P. J. E. and J. T. Yu (Dec. 1970). "Primeval Adiabatic Perturbation in an Expanding Universe". *The Astrophysical Journal* 162, p. 815.

Penzias, A. A. and R. W. Wilson (July 1965). "A Measurement of Excess Antenna Temperature at 4080 Mc/s." *The Astrophysical Journal* 142, pp. 419–421.

Planck Collab., P. A. R. Ade, et al. (Sept. 2016). "Planck 2015 results". *Astronomy & Astrophysics* 594, A13.

Planck Collab., N. Aghanim, et al. (Sept. 2020). "Planck 2018 results". *Astronomy & Astrophysics* 641, A6.

Planck Collab., Akrami, Y., et al. (2020). "Planck 2018 results - IV. Diffuse component separation". *A&A* 641, A4.

Planelles, S., D. R. G. Schleicher, and A. M. Bykov (Apr. 2014). "Large-Scale Structure Formation: From the First Non-linear Objects to Massive Galaxy Clusters". *Space Science Reviews* 188.1-4, pp. 93–139.

Quinn, T., N. Katz, J. Stadel, and G. Lake (1997). *Time stepping N-body simulations*.

Roos, M. (2012). "Astrophysical and Cosmological Probes of Dark Matter". *Journal of Modern Physics* 03.09, pp. 1152–1171.

Springel, V. (Dec. 2005). "The cosmological simulation code gadget-2". *Monthly Notices of the Royal Astronomical Society* 364.4, pp. 1105–1134.

Stefanon, M. et al. (Nov. 2021). "Galaxy Stellar Mass Functions from z 10 to z 6 using the Deepest Spitzer/Infrared Array Camera Data: No Significant Evolution in the Stellar-to-halo Mass Ratio of Galaxies in the First Gigayear of Cosmic Time". *The Astrophysical Journal* 922.1, 29, p. 29.

Tamm, A., E. Tempel, P. Tenjes, O. Tihhonova, and T. Tuvikene (Sept. 2012). "Stellar mass map and dark matter distribution in M 31". *Astronomy & Astrophysics* 546, A4.

Tillson, H., L. Miller, and J. Devriendt (Aug. 2011). "The environment and redshift dependence of accretion on to dark matter haloes and subhaloes". *Monthly Notices of the Royal Astronomical Society* 417.1, pp. 666–680.

Velten, H. E. S., R. F. vom Marttens, and W. Zimdahl (Nov. 2014). "Aspects of the cosmological "coincidence problem"". *The European Physical Journal C* 74.11.

Wechsler, R. H. and J. L. Tinker (Sept. 2018). "The Connection Between Galaxies and Their Dark Matter Halos". *Annual Review of Astronomy and Astrophysics* 56.1, pp. 435–487.

Weinberg, S. (2008). *Cosmology*. Oxford University Press.